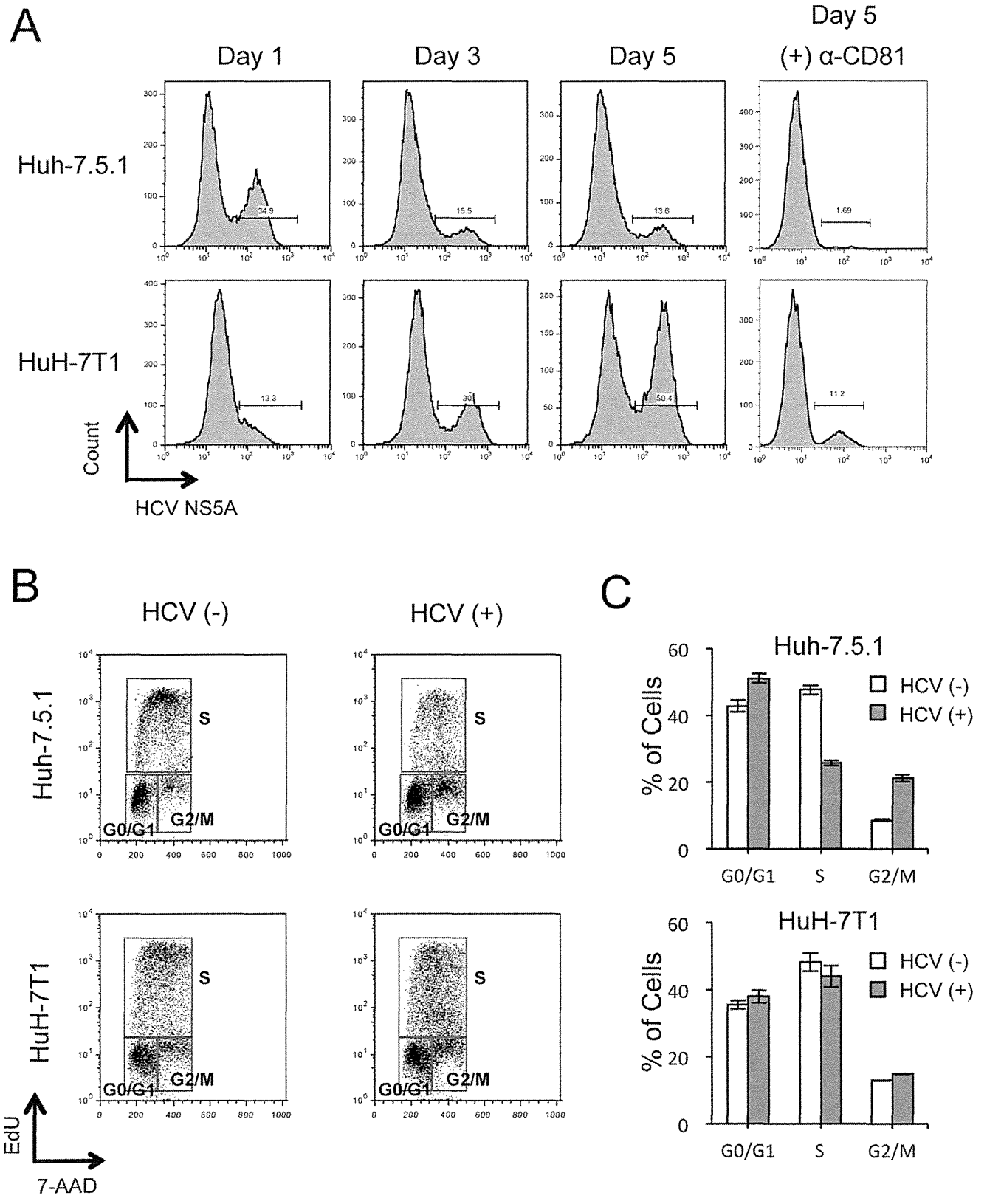

Figure 4. Effects of HCV replication on cell proliferation of Huh-7.5.1 and HuH-7T1. (A) Population of HCV-positive cells after JFH-1 RNA transfection. Two micrograms of JFH-1 RNA was electroporated into Huh-7.5.1 and HuH-7T1 and cultured with or without 10 mg/mL of anti-CD81 antibody (clone JS-81, BD). Cells were harvested at Days 1, 3, and 5. After fixing, cells were stained with anti-NS5A antibody and analyzed by flow cytometry. (B, C) Cell cycle distribution of HCV-positive and -negative cells after JFH-1 RNA transfection. Two micrograms of JFH-1 RNA was electroporated into Huh-7.5.1 and HuH-7T1. Cells were pulse-labeled with EdU and analyzed for cell cycle distribution. The percentages of cells in G0/

G1, S, and G2/M phases of the cell cycle were calculated by gating with FlowJo software. (B) Representative cell cycle distributions of HCV-negative and -positive cells. (C) Percentages of cells in each phase of the cell cycle for HCV-negative and -positive populations. Assays were performed three times independently; data are presented as mean ± standard deviation.
doi:10.1371/journal.pone.0052697.g004

retroviral particles harboring the HCV envelope protein and a luciferase reporter gene, and measures infection efficiency in the absence of HCV replication [11]. The infectivity titer of HCVcc in HuH-7T1 was 33.0%±8.1% of that in Huh-7.5.1 (Fig. 2A). To evaluate the infection efficiency of HCVpp, cellular luciferase activity was measured after HCVpp infection. The luciferase activity in HuH-7T1 was 39.5%±9.0% of that in Huh-7.5.1 (Fig. 2B). As there were differences in infection efficiencies of HCVcc and HCVpp between these cell lines, we analyzed cell-surface expression of the HCV receptor, CD81, using flow cytometry. The population of CD81-expressing cells was slightly lower in HuH-7T1 than in Huh-7.5.1, and HuH-7T1 showed a broad peak of CD81 expression, indicating that CD81 expression level in each cell varied (Fig. S2). Taken together, these results indicated that the susceptibility for HCV infection in HuH-7T1 was lower than in Huh-7.5.1. This distinction presumably reflected the reduced population of CD81-expressing cells, implying that this step was not responsible for the enhanced virus production in HuH-7T1.

We assessed RNA replication efficiency by transfection with a subgenomic JFH-1 replicon RNA that harbored a luciferase-encoding gene. Subgenomic replicon assay revealed that RNA replication in HuH-7T1 demonstrated similar kinetics to that seen in Huh-7.5.1 when compared with the fold-increase value over 4 h of each cells (Fig. 3A), but the absolute luciferase activities of HuH-7T1 were lower than that of Huh-7.5.1 at all time points tested (Fig. S3). We then compared RNA transfection efficiency by measuring the RNA titers of the transfected replication-defective subgenomic replicon RNA (SGR-JFH1/GND-Luc) in the cells. The amount of replicon RNA in the two cell lines was same level at 4 h after transfection (Fig. 3B). However, the luciferase activity in HuH-7T1 was 2.9-times lower than that of Huh-7.5.1 at 4 h after transfection (Fig. 3C). Thus, translation efficiency of HCV genome was lower in HuH-7T1 than in Huh-7.5.1. Taken together, neither the translation or replication step was responsible for enhanced virus production in HuH-7T1.

To assess the efficiencies of intracellular infectious virus production and secretion, we compared infectivity titers in cells and medium of JFH-1 RNA-transfected HuH-7T1 and Huh-7.5.1. At Day 5 after transfection, the intracellular infectivity of HuH-7T1 was 83-fold higher than that of Huh-7.5.1 (Table 1). However, the core protein level of the cells of HCV RNA-transfected HuH-7T1 at Day 5 was only 2.9-fold higher than that of Huh-7.5.1 (Fig. 1B), indicating that infectious HCV particles were assembled more efficiently in HuH-7T1 than in Huh-7.5.1. Virus secretion efficiencies also were assessed by comparing the ratio of infectivity titers in cells and supernatants, and were 3.7-fold lower in HuH-7T1 compared to Huh-7.5.1 (Table 1). Taken together, these results indicated that the efficiency of intracellular infectious virus production was significantly higher in HuH-7T1 than that in Huh-7.5.1, whereas virus secretion efficiency was slightly lower in HuH-7T1 than that in Huh-7.5.1. Therefore, the enhanced intracellular infectious virus production was considered to be responsible for the advantage of HuH-7T1.

Gene expression analysis

To identify the host factors regarding the concerned properties of HuH-7T1, we measured gene expression levels for genes that encode cellular factors reported to be involved in the HCV life cycle. Among 37 host factor-encoding transcripts tested, none except for miR-122 showed more than 2-fold higher or lower expression levels in HuH-7T1 compared to Huh-7.5.1 (Fig. S4). The gene expression level of miR-122 was approximately 5-times lower in HuH-7T1 than in Huh-7.5.1.

Cell cycle analysis of HuH-7T1 and Huh-7.5.1

Although we found that intracellular infectious HCV particles produced more efficiently in HuH-7T1 than in Huh-7.5.1, we thought that there were other possible steps associated with the efficient virus production of HuH-7T1. Because, when HCV RNA is transfected, HuH-7T1 forms the larger HCV positive cell clusters than Huh-7.5.1 (Fig. 1G), although viral entry is less

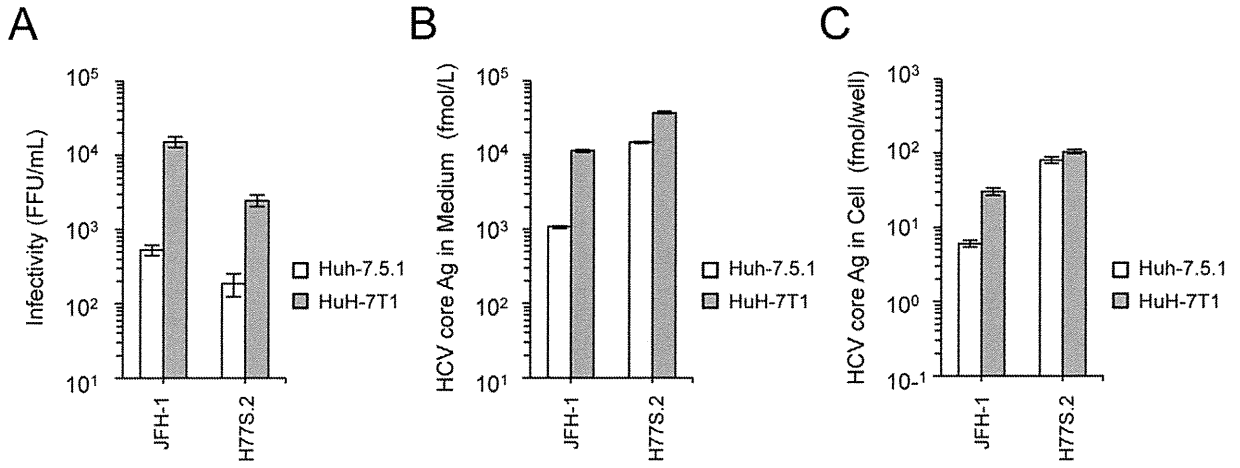

Figure 5. Infectious virus production of H77S.2 in HuH-7T1 and Huh-7.5.1. Two micrograms of JFH-1 RNA or 10 micrograms of H77S.2 RNA were electroporated into Huh-7.5.1 and HuH-7T1. Culture medium and cells were harvested at Day 3, and infectivity titer and HCV core level were determined.
doi:10.1371/journal.pone.0052697.g005

efficient in HuH-7T1 as compared with Huh-7.5.1. To determine other advantages of HuH-7T1, we used flow cytometry to monitor the population of the HCV-positive cells after RNA transfection. At Day 1, the population of HCV-positive cells was higher in Huh-7.5.1 (34.9%) than in HuH-7T1 (13.3%) (Fig. 4A). However, the population of HCV-positive cells in HuH-7T1 increased from Day 1 to Day 5, while that in Huh-7.5.1 decreased over the same interval. When we added anti-CD81 antibody to the medium to exclude the effect of re-infection of the progeny virus, we found that the population of HCV-positive cells in HuH-7T1 did not change from Day 1 to Day 5, while that in Huh-7.5.1 decreased more severely. From these data, we hypothesized that proliferation of HCV-positive cells differed between these cell lines. To clarify this point, we compared the cell cycle distribution of HCV-positive and -negative cells after JFH-1 RNA transfection (Fig. 4B). In Huh-7.5.1, the fraction of cells in S phase was lower among HCV-positive cells than among HCV-negative cells (25.7%±0.8% vs 47.6%±1.5%, respectively; $P<0.05$; Fig. 5C); conversely, the fraction of cells in G0/G1 and G2/M phases was higher among HCV-positive cells compared to HCV-negative cells (51.0%±1.4% vs. 42.8%±1.7%, 21.2%±1.1% vs. 8.6%±0.4%, respectively; $P<0.05$, Fig. 4C), indicating that cell proliferation was suppressed by HCV replication in Huh-7.5.1. By contrast, in HuH-7T1, the fraction of cells in S phase was not significantly different for HCV-positive and -negative cells (Fig. 4C). Thus, unlike Huh-7.5.1, HuH-7T1 evaded the cell cycle arrest associated with HCV replication.

We also analyzed HCV-related apoptosis by terminal deoxynucleotidyl transferase-mediated deoxyuridine triphosphate nick-end labeling (TUNEL) assay and found that apoptosis was observed in a limited number of HCV-positive cells (Fig. S5) as we reported previously [17].

Comparisons of virus production level of H77S.2 (genotype 1a) between HuH-7T1 and Huh-7.5.1

To test whether HuH-7T1 could enhance viral production of HCV strains other than JFH-1, we transfected H77S.2 RNA into HuH-7T1 and Huh-7.5.1 and compared the infectious virus production. As seen with JFH-1 RNA transfection, H77S.2 RNA transfection of HuH-7T1 resulted in increased (13.1-fold) levels of infectious virus and increased (2.5-fold) level of HCV core in medium compared to Huh-7.5.1 (Fig. 5A and 5B), although intracellular HCV core was slightly higher in HuH-7T1 than in Huh-7.5.1 (Fig. 5C).

Discussion

Increased efficiency of virus production can be achieved by viral adaptations associated with enhancement of steps in the viral life cycle. A number of adaptive mutations that could enhance viral genome replication or viral particle assembly has been reported, although the effects of some of these mutations were strain specific [18,19], and none of these has been reported to be applicable to multiple strains and genotypes. Therefore, to obtain the efficient virus production with multiple HCV strains, several cell lines permissive for HCV have been established [6,20,21,22,23]. Generally, they were generated by curing replicon cells in which HCV subgenomic replicon replicated efficiently. As a result, these cured cells support primarily the HCV RNA replication and it is not sufficient to obtain large amounts of virus. The Huh-7.5.1 strain is an example of such a cured cell, and is known to have a loss-of-function mutation in the gene encoding RIG-I, thereby impairing a part of innate immune system and permitting increased HCV replication [20,24]. In the present study, we used another strategy to obtain the cell line for efficient HCV production, namely the use of limiting dilution to isolate a cell line with the desired properties. Our resulting cell line (designated HuH-7T1) produced infectious virus more efficiently than Huh-7.5.1, while supporting a more rapid increase of HCV infected cells.

To identify the affected steps of the viral life cycle in HuH-7T1, we systematically used various assays to investigate the steps of viral infection, translation, replication, infectious viral particle production, and secretion. The HCV infection step was assessed by two assays, using HCVcc and HCVpp. Both assays indicated that the HCV infection efficiency was lower in HuH-7T1 than in Huh-7.5.1. It has been reported that the susceptibility for HCV infection was associated with CD81 expression levels [11,25]. We observed that the population of CD81-expressing cells was lower in HuH-7T1 than in Huh-7.5.1. Therefore, the lower infection efficiency of HuH-7T1 was probably due to the reduced number of CD81-expressing cells. We found that the efficiency of genome translation was lower, but the efficiency of replication was similar in HuH-7T1 compared with Huh-7.5.1. By the gene expression analysis, miR-122 was detected as less expressed in HuH-7T1, and it may be responsible for the lower translation efficiency of HuH-7T1. In contrast, the efficiency of intracellular infectious viral particle production was substantially higher in HuH-7T1 than in Huh-7.5.1. We measured the expression levels of genes encoding host factors involved in viral particle assembly, but did not identify any responsible genes for HuH-7T1 phenotype. A comprehensive microarray analysis would be needed to determine the responsible host factors. We also found that virus secretion efficiency was lower in HuH-7T1 than in Huh-7.5.1. Nevertheless, virus production in HuH-7T1 was significantly higher than that in Huh-7.5.1, suggesting that the enhancement of intracellular viral particle production efficiency in HuH-7T1 was sufficient to overcome other disadvantages compared to Huh-7.5.1.

Immunostaining analysis clearly indicated that the number of HCV-positive cells at Day 5 after RNA transfection was larger for HuH-7T1 than for Huh-7.5.1, and the percentage of HCV positive cell clusters consisting of more than 5 cells was higher in HuH-7T1 than in Huh-7.5.1. These effects may not be fully explained by the difference in intracellular viral particle production efficiency. Thus, we focused on the cell proliferation of HCV-replicating cells in HuH-7T1 and Huh-7.5.1. Flow cytometry analysis revealed that the HCV-positive cell population increased in HuH-7T1 from Day 1 to Day 5, in contrast to the decrease seen in Huh-7.5.1 cells during the same interval. A detailed analysis of the cell cycle populations revealed that the ratio of S-phase cells was reduced by HCV replication in Huh-7.5.1, but not in HuH-7T1. Thus, cell proliferation was suppressed by HCV replication in Huh-7.5.1, but not in HuH-7T1. The time-dependent reduction of the HCV-positive cell population observed in Huh-7.5.1 probably resulted from decreased proliferation activity of HCV-replicating cells relative to HCV-negative cells in spite of the efficient re-infection of the progeny virus. In the case of HuH-7T1, the HCV-positive cells could proliferate as like as the HCV-negative cells, and as a result, the HCV-positive cell population was increased by the re-infection of the progeny virus allowing production of large amounts of viruses.

Cell cycle arrest associated with HCV replication in cell culture has been reported previously. Walters et al. observed S-phase reduction in Huh7.5 cells infected with J6/JFH-1 chimeric viruses, but could not identify the factor(s) responsible for the delay in cell cycle progression [26,27]. Another group also reported an increase in G2/M phase and reduction in S phase in Huh7.5 cells following transfection of JFH-1 and its chimeric viral RNA, and suggested

that the degree of cell cycle arrest was related to the intracellular level of viral protein [26,27]. Additionally, there are numerous papers reporting the relationship between cell cycle arrest and individual HCV proteins such as core [28,29,30], NS2 [31] and NS5B [32,33,34]. However, effects of these HCV proteins on cell cycle remain controversial, and the mechanisms of cell cycle arrest caused by HCV replication remain unclear. Since HuH-7T1 are resistant to cell cycle arrest by HCV replication while Huh-7.5.1 are sensitive, these cell lines should help to clarify the mechanism of cell cycle arrest while facilitating the identification of host and viral factors involved therein.

The improved viral production in the HuH-7T1 was observed also with another HCV strain, H77S.2. This viral strain is a derivative of H77S [35], which is genotype 1a and produces infectious virus in cultured cells following full-genome RNA transfection [13]. Although the H77S.2 strain could replicate, and secreted HCV core protein more efficiently than JFH-1 in Huh-7.5.1, infectious virus production was less efficient as compared with JFH-1 and infectivity in the medium of H77S.2 RNA-transfected Huh-7.5.1 was at a detectable level. These data implied that H77S.2 mainly secreted unassembled HCV core proteins or noninfectious virus particles. In HuH-7T1, the infectious virus production of H77S.2 was enhanced about ten times, and HCV core level in the medium was enhanced about three times, indicating that HuH-7T1 enhanced infectious virus production. These data also indicated that large amounts of infectious viruses could also be obtained with other HCV strains in HuH-7T1.

In conclusion, we isolated a HuH-7 subclone, HuH-7T1, that displays improved ability to produce infectious HCV virus particles. Enhanced intracellular infectious virus production and evasion of cell cycle arrest were important for the increased efficiency of viral production. This cell line is expected to facilitate HCV research both by providing increased amounts of HCV particles and by permitting the identification of cellular factors involved in viral particle production.

Supporting Information

Figure S1 Kinetics of JFH-1 virus infection on HuH-7T1, huh-7.5.1 and HuH-7. Target cells were seeded into 12-well plates at a density of 2×10^5 cells/well. On the following day, the cells were infected with JFH-1 virus at a multiplicity of infection of 0.1 and incubated for 72 h at 37°C. Culture medium and cells were harvested at Days 1, 3, and 5, and HCV core protein levels in the culture medium and in the cells were measured. Assays were performed three times independently, and data are presented as mean ± standard deviation.
(TIF)

Figure S2 Expression levels of CD81 in HuH-7T1 and Huh-7.5.1. Analysis of CD81 expression on cell surface of HuH-7T1 and Huh-7.5.1 by flow cytometry. The assays were performed three times independently; representative data are shown. Percentages of CD81-positive cells are shown above the histogram.
(TIF)

Figure S3 Comparison of absolute luciferase activity in HuH-7T1 and Huh-7.5.1. Absolute measurement data of luciferase activity at Fig. 3A was plotted.
(TIF)

Figure S4 Expression levels of genes associated with HCV life cycle in HuH-7T1 and Huh-7.5.1. Total cellular RNA was extracted from Huh-7.5.1 and HuH-7T1, and cDNA was synthesized using Superscript III reverse transcriptase (except for miR-122) or TaqMan MicroRNA RT Kit (miR-122). Quantitative PCR was performed using gene-specific primer and probe sets. Data are expressed as a fold-difference of expression compared to that in Huh-7.5.1. Dashed lines indicate 2-fold higher or lower expression levels compared to Huh-7.5.1.
(TIF)

Figure S5 Apoptosis assay of JFH-1 RNA-transfected cells. Two micrograms of JFH-1 RNA was electroporated into Huh-7.5.1 and HuH-7T1. Cells were harvested at Day 3 and fixed in 4% paraformaldehyde, permeabilized, and stained with anti-NS5A antibody (clone KS0265-1) and Alexa Fluor 647 Goat Anti-mouse IgG (Invitrogen). Apoptosis was detected by terminal deoxynucleotidyl transferase-mediated deoxyuridine triphosphate nick-end labeling (TUNEL). Samples were analyzed using a FACS Calibur flow cytometer.
(TIF)

Text S1 Supporting Materials and Methods.
(DOC)

Acknowledgments

The authors wish to thank Dr. Francis V. Chisari (Scripps Research Institute, La Jolla, CA) for providing the Huh-7.5.1 cell line, and Dr. Stanley M. Lemon (University of North Carolina at Chapel Hill, Chapel Hill, NC) for providing pH77S.2.

Author Contributions

Conceived and designed the experiments: AM TW SM TK. Performed the experiments: AM NS SY MIS TM SK TK. Analyzed the data: AM TK. Contributed reagents/materials/analysis tools: SY MIS SM. Wrote the paper: AM SM TK.

References

1. Choo QL, Kuo G, Weiner AJ, Overby LR, Bradley DW, et al. (1989) Isolation of a cDNA clone derived from a blood-borne non-A, non-B viral hepatitis genome. Science 244: 359–362.
2. Kiyosawa K, Sodeyama T, Tanaka E, Gibo Y, Yoshizawa K, et al. (1990) Interrelationship of blood transfusion, non-A, non-B hepatitis and hepatocellular carcinoma: analysis by detection of antibody to hepatitis C virus. Hepatology 12: 671–675.
3. Liang TJ, Rehermann B, Seeff LB, Hoofnagle JH (2000) Pathogenesis, natural history, treatment, and prevention of hepatitis C. Ann Intern Med 132: 296–305.
4. Feld JJ, Liang TJ (2006) Hepatitis C – identifying patients with progressive liver injury. Hepatology 43: S194–206.
5. Wakita T, Pietschmann T, Kato T, Date T, Miyamoto M, et al. (2005) Production of infectious hepatitis C virus in tissue culture from a cloned viral genome. Nat Med 11: 791–796.
6. Zhong J, Gastaminza P, Cheng G, Kapadia S, Kato T, et al. (2005) Robust hepatitis C virus infection in vitro. Proc Natl Acad Sci U S A 102: 9294–9299.
7. Lindenbach BD, Evans MJ, Syder AJ, Wolk B, Tellinghuisen TL, et al. (2005) Complete replication of hepatitis C virus in cell culture. Science 309: 623–626.
8. Nakabayashi H, Taketa K, Miyano K, Yamane T, Sato J (1982) Growth of human hepatoma cells lines with differentiated functions in chemically defined medium. Cancer Res 42: 3858–3863.
9. Lohmann V, Korner F, Koch J, Herian U, Theilmann L, et al. (1999) Replication of subgenomic hepatitis C virus RNAs in a hepatoma cell line. Science 285: 110–113.
10. Sainz B Jr., Barretto N, Uprichard SL (2009) Hepatitis C virus infection in phenotypically distinct Huh7 cell lines. PLoS One 4: e6561.
11. Akazawa D, Date T, Morikawa K, Murayama A, Miyamoto M, et al. (2007) CD81 expression is important for the permissiveness of Huh7 cell clones for heterogeneous hepatitis C virus infection. J Virol 81: 5036–5045.
12. Kato T, Date T, Miyamoto M, Sugiyama M, Tanaka Y, et al. (2005) Detection of anti-hepatitis C virus effects of interferon and ribavirin by a sensitive replicon system. J Clin Microbiol 43: 5679–5684.

13. Shimakami T, Welsch C, Yamane D, McGivern DR, Yi M, et al. (2011) Protease inhibitor-resistant hepatitis C virus mutants with reduced fitness from impaired production of infectious virus. Gastroenterology 140: 667–675.
14. Kato T, Date T, Murayama A, Morikawa K, Akazawa D, et al. (2006) Cell culture and infection system for hepatitis C virus. Nat Protoc 1: 2334–2339.
15. Murayama A, Weng L, Date T, Akazawa D, Tian X, et al. (2010) RNA polymerase activity and specific RNA structure are required for efficient HCV replication in cultured cells. PLoS Pathog 6: e1000885.
16. Murayama A, Kato T, Akazawa D, Sugiyama N, Date T, et al. (2011) Production of infectious chimeric hepatitis C virus genotype 2b harboring minimal regions of JFH-1. J Virol 86: 2143–2152.
17. Saeed M, Shiina M, Date T, Akazawa D, Watanabe N, et al. (2011) In vivo adaptation of hepatitis C virus in chimpanzees for efficient virus production and evasion of apoptosis. Hepatology 54: 425–433.
18. Gu B, Gates AT, Isken O, Behrens SE, Sarisky RT (2003) Replication studies using genotype 1a subgenomic hepatitis C virus replicons. J Virol 77: 5352–5359.
19. Takeda M, Ikeda M, Ariumi Y, Wakita T, Kato N (2012) Development of Hepatitis C Virus Production Reporter Assay Systems Using Two Different Hepatoma Cell Lines. J Gen Virol.
20. Blight KJ, McKeating JA, Rice CM (2002) Highly permissive cell lines for subgenomic and genomic hepatitis C virus RNA replication. J Virol 76: 13001–13014.
21. Friebe P, Boudet J, Simorre JP, Bartenschlager R (2005) Kissing-loop interaction in the 3′ end of the hepatitis C virus genome essential for RNA replication. J Virol 79: 380–392.
22. Ikeda M, Abe K, Dansako H, Nakamura T, Naka K, et al. (2005) Efficient replication of a full-length hepatitis C virus genome, strain O, in cell culture, and development of a luciferase reporter system. Biochem Biophys Res Commun 329: 1350–1359.
23. Robinson M, Yang H, Sun SC, Peng B, Tian Y, et al. (2010) Novel hepatitis C virus reporter replicon cell lines enable efficient antiviral screening against genotype 1a. Antimicrob Agents Chemother 54: 3099–3106.
24. Sumpter R Jr., Loo YM, Foy E, Li K, Yoneyama M, et al. (2005) Regulating intracellular antiviral defense and permissiveness to hepatitis C virus RNA replication through a cellular RNA helicase, RIG-I. J Virol 79: 2689–2699.
25. Koutsoudakis G, Herrmann E, Kallis S, Bartenschlager R, Pietschmann T (2007) The level of CD81 cell surface expression is a key determinant for productive entry of hepatitis C virus into host cells. J Virol 81: 588–598.
26. Kannan RP, Hensley LL, Evers LE, Lemon SM, McGivern DR (2011) Hepatitis C virus infection causes cell cycle arrest at the level of initiation of mitosis. J Virol 85: 7989–8001.
27. Walters KA, Syder AJ, Lederer SL, Diamond DL, Paeper B, et al. (2009) Genomic analysis reveals a potential role for cell cycle perturbation in HCV-mediated apoptosis of cultured hepatocytes. PLoS Pathog 5: e1000269.
28. Yao ZQ, Eisen-Vandervelde A, Ray S, Hahn YS (2003) HCV core/gC1qR interaction arrests T cell cycle progression through stabilization of the cell cycle inhibitor p27Kip1. Virology 314: 271–282.
29. Alisi A, Mele R, Spaziani A, Tavolaro S, Palescandolo E, et al. (2005) Thr 446 phosphorylation of PKR by HCV core protein deregulates G2/M phase in HCC cells. J Cell Physiol 205: 25–31.
30. Spaziani A, Alisi A, Sanna D, Balsano C (2006) Role of p38 MAPK and RNA-dependent protein kinase (PKR) in hepatitis C virus core-dependent nuclear delocalization of cyclin B1. J Biol Chem 281: 10983–10989.
31. Yang XJ, Liu J, Ye L, Liao QJ, Wu JG, et al. (2006) HCV NS2 protein inhibits cell proliferation and induces cell cycle arrest in the S-phase in mammalian cells through down-regulation of cyclin A expression. Virus Res 121: 134–143.
32. Munakata T, Nakamura M, Liang Y, Li K, Lemon SM (2005) Down-regulation of the retinoblastoma tumor suppressor by the hepatitis C virus NS5B RNA-dependent RNA polymerase. Proc Natl Acad Sci U S A 102: 18159–18164.
33. Naka K, Dansako H, Kobayashi N, Ikeda M, Kato N (2006) Hepatitis C virus NS5B delays cell cycle progression by inducing interferon-beta via Toll-like receptor 3 signaling pathway without replicating viral genomes. Virology 346: 348–362.
34. Wang Y, Xu Y, Tong W, Pan T, Li J, et al. (2011) Hepatitis C virus NS5B protein delays s phase progression in human hepatocyte-derived cells by relocalizing cyclin-dependent kinase 2-interacting protein (CINP). J Biol Chem 286: 26603–26615.
35. Yi M, Villanueva RA, Thomas DL, Wakita T, Lemon SM (2006) Production of infectious genotype 1a hepatitis C virus (Hutchinson strain) in cultured human hepatoma cells. Proc Natl Acad Sci U S A 103: 2310–2315.

PLOS ONE

A Novel Rabbit Immunospot Array Assay on a Chip Allows for the Rapid Generation of Rabbit Monoclonal Antibodies with High Affinity

Tatsuhiko Ozawa[1☯], Xiuhong Piao[1☯], Eiji Kobayashi[1], Yue Zhou[2], Hiroaki Sakurai[2], Tsugunobu Andoh[3], Aishun Jin[1,4], Hiroyuki Kishi[1]*, Atsushi Muraguchi[1]

1 Department of Immunology, Graduate School of Medicine and Pharmaceutical Sciences, University of Toyama, Toyama, Japan, **2** Department of Cancer Cell Biology, Graduate School of Medicine and Pharmaceutical Sciences, University of Toyama, Toyama, Japan, **3** Department of Applied Pharmacology, Graduate School of Medicine and Pharmaceutical Sciences, University of Toyama, Toyama, Japan, **4** Department of Immunology, College of Basic Medical Sciences, Harbin Medical University, Nangang District, Harbin, China

Abstract

Antigen-specific rabbit monoclonal antibodies (RaMoAbs) are useful due to their high specificity and high affinity, and the establishment of a comprehensive and rapid RaMoAb generation system has been highly anticipated. Here, we present a novel system using immunospot array assay on a chip (ISAAC) technology in which we detect and retrieve antigen-specific antibody-secreting cells from the peripheral blood lymphocytes of antigen-immunized rabbits and produce antigen-specific RaMoAbs with 10^{-12} M affinity within a time period of only 7 days. We have used this system to efficiently generate RaMoAbs that are specific to a phosphorylated signal-transducing molecule. Our system provides a new method for the comprehensive and rapid production of RaMoAbs, which may contribute to laboratory research and clinical applications.

Citation: Ozawa T, Piao X, Kobayashi E, Zhou Y, Sakurai H, et al. (2012) A Novel Rabbit Immunospot Array Assay on a Chip Allows for the Rapid Generation of Rabbit Monoclonal Antibodies with High Affinity. PLoS ONE 7(12): e52383. doi:10.1371/journal.pone.0052383

Editor: Srinivas Kaveri, Cordelier Research Center, INSERMU872-Team16, France

Received July 31, 2012; **Accepted** November 12, 2012; **Published** December 26, 2012

Funding: Vivalis; The funders had no role in study design, data collection and analysis, decision to publish, or preparation of the manuscript.

Competing Interests: AM was supported by a research fund from Vivalis (Nantes, France.) The ISAAC method is covered by patents that have been exclusively licensed to Vivalis (Nantes, France.) Patent details: Pub.No.: WO/2009/017226, International Application No.: PCT/JP2008/063874, Title: CELL SCREENING METHOD; HK is one of Scientific Advisory Board Members of Vivalis. Microwell array chips are now provided to us by Vivalis. There are no further patents, products in development or marketed products to declare. This does not alter the authors' adherence to all the PLOS ONE policies on sharing data and materials, as detailed online in the guide for authors.

* E-mail: immkishi@med.u-toyama.ac.jp

☯ These authors contributed equally to this work.

Introduction

Monoclonal antibodies are widely used in laboratory research as well as clinical applications due to their high specificity and high affinity. Notably, compared to conventional rodent antibodies, rabbit monoclonal antibodies (RaMoAbs) are ideal for investigation and diagnosis for two reasons. First, rabbit antibodies generally exhibit a high affinity and high specificity [1–6]. Second, rabbits are known to produce antibodies to many antigens that are not immunogenic in mice or other animals [1,4,7–11].

Mouse-rabbit hetero-hybridomas were initially used to produce RaMoAbs [10,12–14]. However, these hetero-hybridomas were highly unstable, difficult to clone, and unable to secrete antibodies for prolonged periods [2]. In 1995, Knight and colleagues established a plasmacytoma cell line over-expressing v-*abl* and c-*myc*, which they used as a hybridoma partner cell line [6,15]. Nevertheless, the hybridoma method is not widely used at the laboratory level.

We have established a rapid, efficient, and high-throughput system for identifying and recovering objective antibody-secreting cells (ASCs) using microwell array chips and immunospot array assay on a chip (ISAAC) technology [16,17]. Microwell array chip has an array of up to 234,000 wells, and each well has a size and shape that are optimized for the accommodation of a single lymphocyte; this feature has enabled us to analyze live cells on a single-cell basis. The ISAAC system can detect antigen-specific ASCs in human peripheral blood lymphocytes (PBLs) and can produce antigen-specific human monoclonal antibodies within 7 days.

In this study, we used the ISAAC system to detect antigen-specific antibody-secreting single primary B-cells from rabbits. We demonstrated that the rabbit-ISAAC system allows for the comprehensive and rapid production of RaMoAbs with high affinity. Moreover, the system can produce RaMoAbs that are specific to a phosphorylated signal-transducing molecule. This innovative technology may contribute to the high-throughput production of RaMoAbs for laboratory research and clinical applications.

Results

The Rabbit-ISAAC System

To establish the rabbit-ISAAC system, we first tested the feasibility of the ISAAC system for detecting rabbit ASCs on a single-cell basis. We immunized a rabbit with hen egg lysozyme (HEL) and prepared IgG^+ lymphocytes from PBLs (Figure 1A). We then arrayed IgG^+ cells on a HEL-coated chip and detected

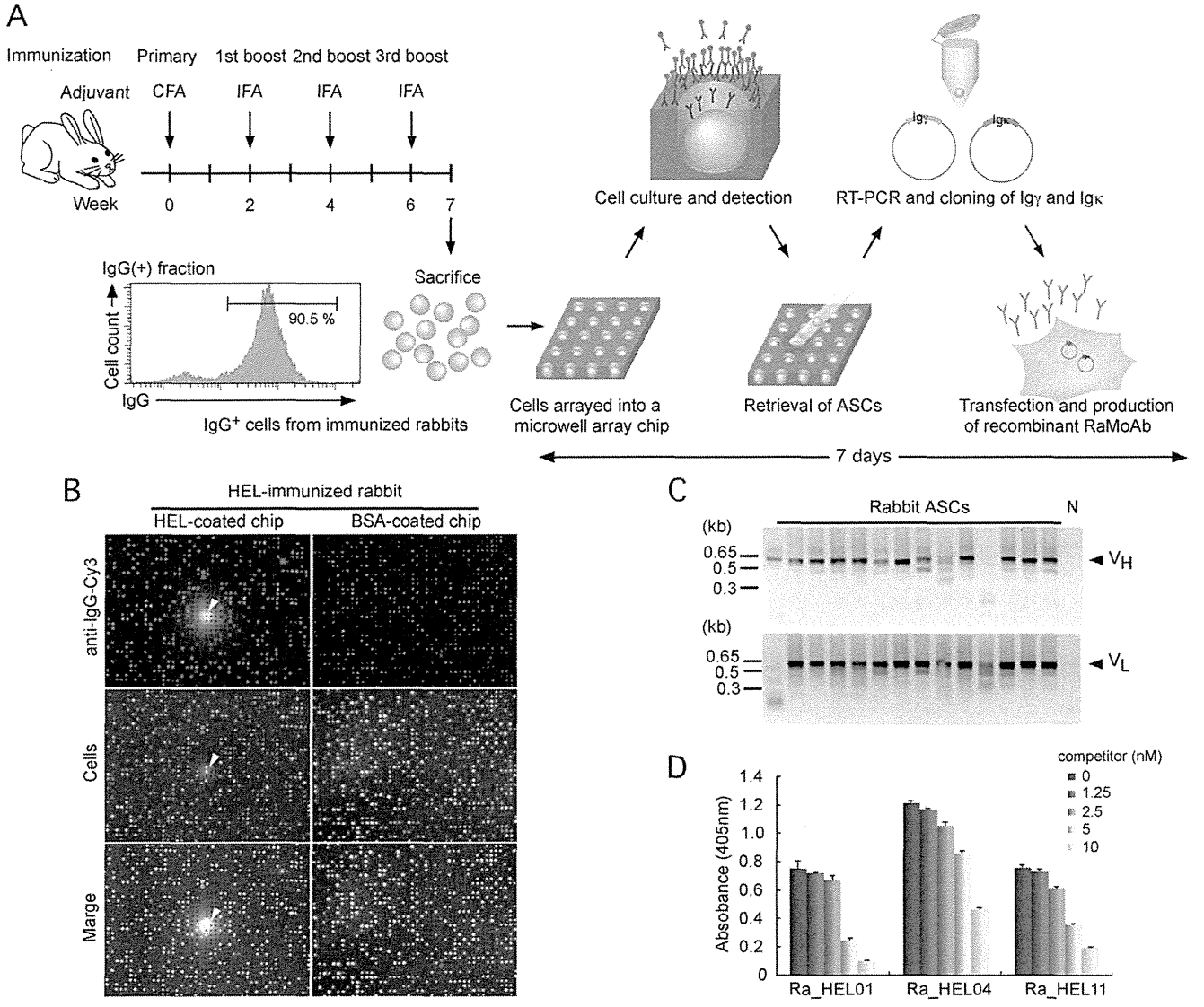

Figure 1. The rabbit-ISAAC system. (A) A scheme depicting the rabbit-ISAAC procedure. Briefly, rabbits were immunized and later sacrificed 1 week after the final boost. Rabbit IgG^+ cells were sorted, and single antigen-specific ASCs were detected using a microwell array chip. Next, rabbit immunoglobulin cDNAs were amplified from single cells, cloned into expression vectors and co-transduced into CHO-S cells. The antigen specificity of the produced antibodies can be determined 7 days after the detection of antigen-specific ASCs on the microwell array chip. (B) Detection of single HEL-specific ASCs in PBLs from HEL-immunized rabbits by the rabbit-ISAAC technique. Antibody secretion was detected with HEL (top left) or BSA (negative control, top right). The cells were then stained with Oregon Green (middle), and the antibody immunospots and cell signals were merged (bottom). Arrowheads indicate HEL-specific ASCs. (C) Amplification of rabbit V_H (top) and V_L (bottom) with a single-cell 5′-RACE procedure. The PCR products were analyzed by agarose gel electrophoresis. Sizes are shown at the left. Each lane shows the 5′-RACE products of individual cells. "N" indicates a cell-free RT-PCR reaction. (D) Competitive ELISA of HEL-specific RaMoAbs. The antigen specificity of antibodies derived from single ASCs using ISAAC was examined by competitive ELISA using varying amounts of HEL. The data represent means ± s.d. of 3 independent experiments.
doi:10.1371/journal.pone.0052383.g001

HEL-specific ASCs using a Cy3-conjugated antibody that was specific to rabbit IgG. The secreted antibodies produced very strong immunospots on the HEL-coated chip that were not observed on the BSA-coated chip (Figure 1B).

We then retrieved 189 single cells that produced HEL-specific IgG immunospots and transferred the individual cells into separate micro-tubes for the amplification of cDNAs encoding the immunoglobulin heavy (H) and light (L) chain variable regions (V_H and V_L). We amplified V_H and V_L cDNAs using a single-cell 5′-RACE method [17–19] with primers for the γ chain and the κ chain (Figure 1C). We amplified 56 pairs of V_H and V_L cDNAs and inserted these into expression vectors that contained the cDNA of the rabbit immunoglobulin constant region (γ or κ chain). Thereafter, we co-transfected both the γ and κ chain expression vectors together in CHO-S cells, which then produced 55 RaMoAbs. An ELISA showed that 24 of 55 antibodies were specific to HEL (Figure 1D, Table 1, and Table S1).

We then analyzed the cDNA sequences of 24 HEL-specific monoclonal antibodies and obtained 21 distinct sequences (Table 1). In agreement with the previous study [4,20–22], all of these sequences contained a single IGVH1 gene, and a majority of the sequences contained J_H4. Our results indicate that the antibody repertoire obtained from the analysis of primary rabbit

Table 1. Characterization of HEL-specific RaMoAbs.

ID	IGHV	IGHD	IGHJ	IGKV	IGKJ	Frequency[a]	*K*D (M)[b]
Ra_HEL01	1S44	2	4	1S47	1–2	3	2.63×10^{-12}
Ra_HEL04	1S44	6	4	1S37	1–2	2	7.00×10^{-12}
Ra_HEL06	1S44	6	4	1S36	1–2	1	1.45×10^{-12}
Ra_HEL07	1S44	6	4	1S36	1–2	1	3.14×10^{-9}
Ra_HEL08	1S44	2	4	1S36	1–2	1	6.09×10^{-10}
Ra_HEL09	1S21	1	4	1S36	1–2	1	4.15×10^{-11}
Ra_HEL10	1S44	2	4	1S36	1–2	1	3.77×10^{-12}
Ra_HEL11	1S44	2	4	1S36	1–2	1	3.93×10^{-12}
Ra_HEL12	1S44	2	2	1S37	1–2	1	2.09×10^{-7}
Ra_HEL13	1S44	2	4	1S64	1–2	1	5.77×10^{-8}
Ra_HEL14	1S43	8	4	1S44	1–2	1	5.06×10^{-11}
Ra_HEL15	1S44	1	4	1S12	1–2	1	8.07×10^{-10}
Ra_HEL16	1S44	6	2	1S36	1–2	1	3.25×10^{-10}
Ra_HEL17	1S44	1	2	1S4	1–2	1	7.12×10^{-7}
Ra_HEL18	1S44	6	4	1S47	1–2	1	1.47×10^{-12}
Ra_HEL19	1S44	2	4	1S42	1–2	1	1.69×10^{-9}
Ra_HEL20	1S44	6	4	1S36	1–2	1	9.60×10^{-11}
Ra_HEL21	1S44	2	4	1S36	1–2	1	1.35×10^{-12}
Ra_HEL22	1S44	6	4	1S10	1–2	1	1.43×10^{-11}
Ra_HEL23	1S44	4	4	1S4	1–2	1	1.72×10^{-9}
Ra_HEL24	1S44	4	6	1S10	1–2	1	2.11×10^{-9}

[a]Frequency indicates numbers of clones showing identical amino acid sequences.
[b]The data are presented as average of at least two experiments.
doi:10.1371/journal.pone.0052383.t001

ASCs using the rabbit-ISAAC system is similar to that obtained with the conventional hybridoma method.

We next measured the affinity of these antibodies by ELISA (Figure S1). The affinity (*K*D) for HEL ranged from 1×10^{-7} to 1×10^{-12} M (Table 1). Interestingly, the *K*D of 14 out of 24 (56%) antibodies for HEL was estimated to be 10^{-10} to 10^{-12} M. The RaMoAbs with extremely high affinity may detect very small amount of antigen. To examine this possibility, we determined the limit of detection (LOD) in ELISA for a RaMoAb with 10^{-12} M affinity (Ra_HEL21) and a mouse HEL-specific antibody (Mo_HEL10) that showed the highest affinity (3.71×10^{-10} M) among mouse HEL-specific antibodies obtained with ISAAC [17]. The calculated LOD of the RaMoAb was approximately 0.4 pM, and that of the mouse antibody was approximately 10 pM (Figure S2). The results demonstrated that the LOD of the RaMoAb of 10^{-12} M affinity was 25-fold lower than that of the mouse antibody.

Relationship between Rabbit-ISAAC Immunospots and Affinities

The selection of antigen-specific antibodies with high affinity is one of the goals for the screening monoclonal antibodies. Adams *et al.* reported that antibodies with high affinity do not diffuse distantly in tumors [23]. Taking this into account, we predicted that rabbit-ISAAC immunospots of antibodies with high affinity might be smaller in diameter compared to immunospots of antibodies with low affinity. Thus, we measured the distance at which the fluorescence intensities of rabbit-ISAAC immunospots were 50% ($D_{1/2}$) (Figure 2A and 2B). Next, we plotted the $D_{1/2}$ and affinities of individual immunospots (Figure 2C). As expected, antibodies with higher affinities had smaller $D_{1/2}$ values; the average *K*D of antibodies with immunospots of $D_{1/2}<60$ was 2.56×10^{-11} M, while the *K*D of antibodies with $D_{1/2}>60$ was 7.34×10^{-10} M (Student's t-test, $p<0.05$) (Figure 2C). The *K*D of 12 out of 15 (80%) antibodies with $D_{1/2}<60$ was between 10^{-10} and 10^{-12} M, while 2 out of 9 (22%) antibodies with $D_{1/2}>60$ had *K*Ds of less than 10^{-10} M (Fisher's test, $p<0.01$) (Figure 2D). These results indicate that antibodies with high affinities do not diffuse far, which is in agreement with Adams *et al.* [23]. Taken together, these findings demonstrate that we can obtain HEL-specific ASCs with high affinities by retrieving cells with $D_{1/2}<60$; however, the $D_{1/2}$ value may differ depending on the antigen as well as the antibody.

An Efficient Screening System for Phosphorylated Peptide-specific RaMoAbs Using Rabbit-ISAAC

We next utilized the rabbit-ISAAC system to screen for ASCs producing antibodies that specifically recognize a phosphorylated peptide. We immunized rabbits with a phosphorylated peptide of human transforming growth factor-β-activated kinase 1 (TAK1), a key kinase regulating pro-inflammatory and innate/acquired immune signaling pathways [24]. Next, we prepared IgG^+ cells from the PBLs of immunized rabbits and arrayed IgG^+ cells on chips that were coated with rabbit IgG-specific antibodies. We attempted to detect Thr-187-phosphorylated TAK1, a critical site for TAK1 activation, (pTAK1)-peptide-specific ASCs using biotinylated pTAK1-peptide and Cy3-conjugated streptavidin (Figure 3). We obtained 64 monoclonal antibodies that bound to pTAK1-peptide. However, 59 of 64 monoclonal antibodies specifically bound not only to pTAK1-peptide but also to TAK1-peptide (Figure 3 and Table S1).

To efficiently screen for ASCs producing antibodies that specifically bind to pTAK1-peptide but not to TAK1-peptide, we first blocked the rabbit-ISAAC immunospots with TAK1-peptide. We then applied biotinylated pTAK1-peptide and Cy3-conjugated streptavidin to detect ASCs that were specific to pTAK1-peptide (Figure 3B). We obtained 19 monoclonal antibodies that bound to pTAK1-peptide. More than 90% (18 of 19) of the monoclonal antibodies specifically bound to pTAK1-peptide and not to TAK1-peptide (Figure 3C and Table S1). The acquisition efficiency of phosphorylated peptide-specific RaMoAbs was significantly improved compared to the non-blocking procedure (Fisher's test, $p<0.001$) (Figure 3C). These results show that the use of the blocking procedure in the rabbit-ISAAC system is very useful for the isolation of monoclonal antibodies that specifically bind to pTAK1-peptide but not to TAK1-peptide.

We determined the affinity of these antibodies by ELISA (Figure S3). The affinity (*K*D) for pTAK1-peptide ranged from 1×10^{-6} to 1×10^{-9} M (Table 2). Sequencing analysis of the cDNA of 23 pTAK1-peptide-specific antibodies revealed eight distinct sequences (Table 2). All of these sequences contained a single IGVH1 gene, as previously reported [20–22]. Regarding J_H, the frequency of J_H4 usage was not so high as that of HEL antibodies.

Functional Characterization of pTAK1-peptide-specific RaMoAbs

Finally, we characterized pTAK1-peptide-specific RaMoAbs using western blot analysis. It is known that over-expression of TAK1 with TAK1 binding protein 1 (TAB1) results in the phosphorylation of TAK1 at Thr-187 [25–27]. To examine whether pTAK1-peptide-specific RaMoAbs specifically detect Thr-187-phosphorylated TAK1, FLAG-tagged TAK1 and HA-

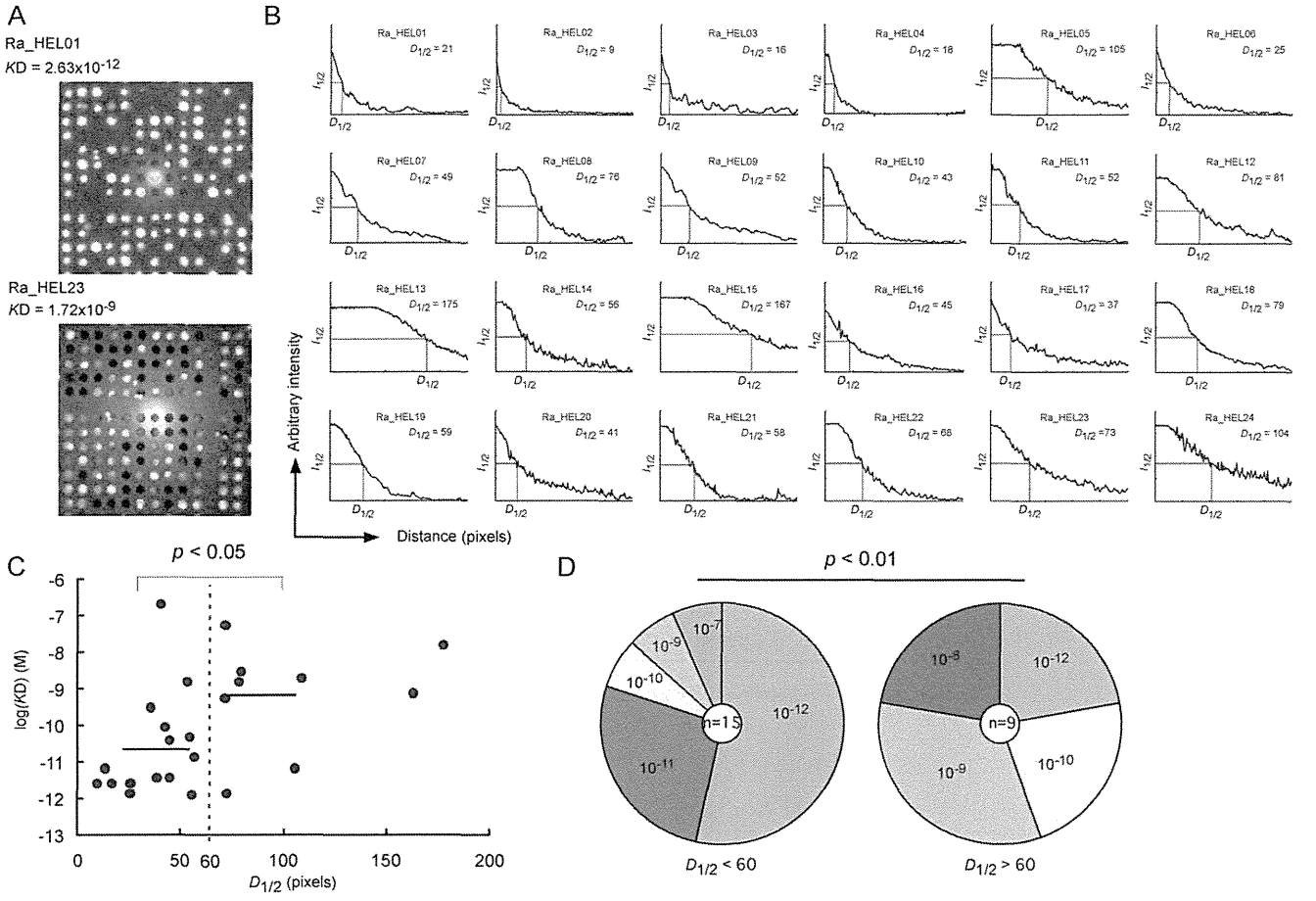

Figure 2. Relationship between rabbit-ISAAC immunospots and affinities. (A) Representative ISAAC immunospots of secreted HEL-binding RaMoAbs with high (*K*D: 10^{-12} M) and low (*K*D: 10^{-9} M) affinity. (B) A decay curve of fluorescence intensities in individual ISAAC immunospots. The fluorescence intensity of individual ISAAC immunospots (*y*-axis) is plotted against the distance (*x*-axis). $I_{1/2}$ is the value at which the immunospot fluorescence intensity reaches 50%, and $D_{1/2}$ indicates the distance at which $I_{1/2}$ is achieved. The $D_{1/2}$ value is shown in each individual plot. (C) Relationship between the $D_{1/2}$ of individual immunospots (*x*-axis) and *K*D (*y*-axis). The dotted line indicates $D_{1/2} = 60$. The bar indicates the average *K*D for antibodies with $D_{1/2}<60$ and those with $D_{1/2}>60$. The *p*-value was determined using Student's t-test. (D) Frequency of antibodies with the indicated order of *K*D values for antibodies with $D_{1/2}<60$ and $D_{1/2}>60$. The colored pie segment indicates the frequency of antibodies with the indicated order of *K*D. The number in the center of the pie chart denotes the number of antibodies analyzed. The *p*-value was determined using Fisher's test.
doi:10.1371/journal.pone.0052383.g002

tagged TAB1 were co-expressed in HeLa cells, and the cell lysates were immunoblotted with pTAK1-peptide-specific antibodies. The phosphorylation-specific band of TAK1 was clearly detected by co-expression with TAB1 (Figure 4A). In contrast, no phosphorylation was detected in the FLAG-tagged alanine-substituted mutant TAK1 (T187A) upon co-expression with TAB1 (Figure 4A).

We next examined whether our pTAK1-peptide-specific RaMoAb detects TNF-α-induced phosphorylation of endogenous TAK1. To this end, HeLa cells were stimulated with TNF-α; subsequently, the cell lysates were immunoblotted with pTAK1-peptide-specific antibodies. Immunoblotting with our Ra_p-TAK23 antibody demonstrated that the bands could be detected in whole cell lysates from TNF-α-treated HeLa cells. Consistent with a previous study [25], the faster migrating bands corresponding to phosphorylated TAK1 were detected 2–5 min after the stimulation (Figure 4B). In contrast, a commercially available antibody could not detect the phosphorylation of endogenous TAK1 (Figure 4B). These results demonstrate that our RaMoAb recognizes Thr-187 phosphorylation of whole TAK1 molecules.

Discussion

In this study, we have demonstrated a novel screening procedure for the production of RaMoAbs using the rabbit-ISAAC system (Figure 1). We demonstrated that the system efficiently produced RaMoAbs with high affinity (10^{-10} *to* 10^{-12} M) (Figure 2 and Table 1). We also demonstrated that the system could efficiently produce RaMoAbs that specifically recognize a phosphorylation-site-specific epitope (Figure 3 and Table 2).

In Table S1, we summarized the efficiency in each experimental step of rabbit ISAAC system. In the absence of blocking, from approximately 20 ml of blood, we obtained approximately 4×10^7 PBL, and obtained 2×10^6 IgG^+ B cells. In the case of HEL, we analyzed a total of approximately 5.5×10^5 IgG^+ cells using 14 microwell array chips (62,500 wells, 15 μm in diameter). As a result, approximately 340 HEL-specific immunospots were detected, and 189 single cells were retrieved. From them, 56 pairs of V_H and V_L cDNAs were amplified and 55 RaMoAbs were produced. Finally, 24 of them specifically bound to HEL. In the

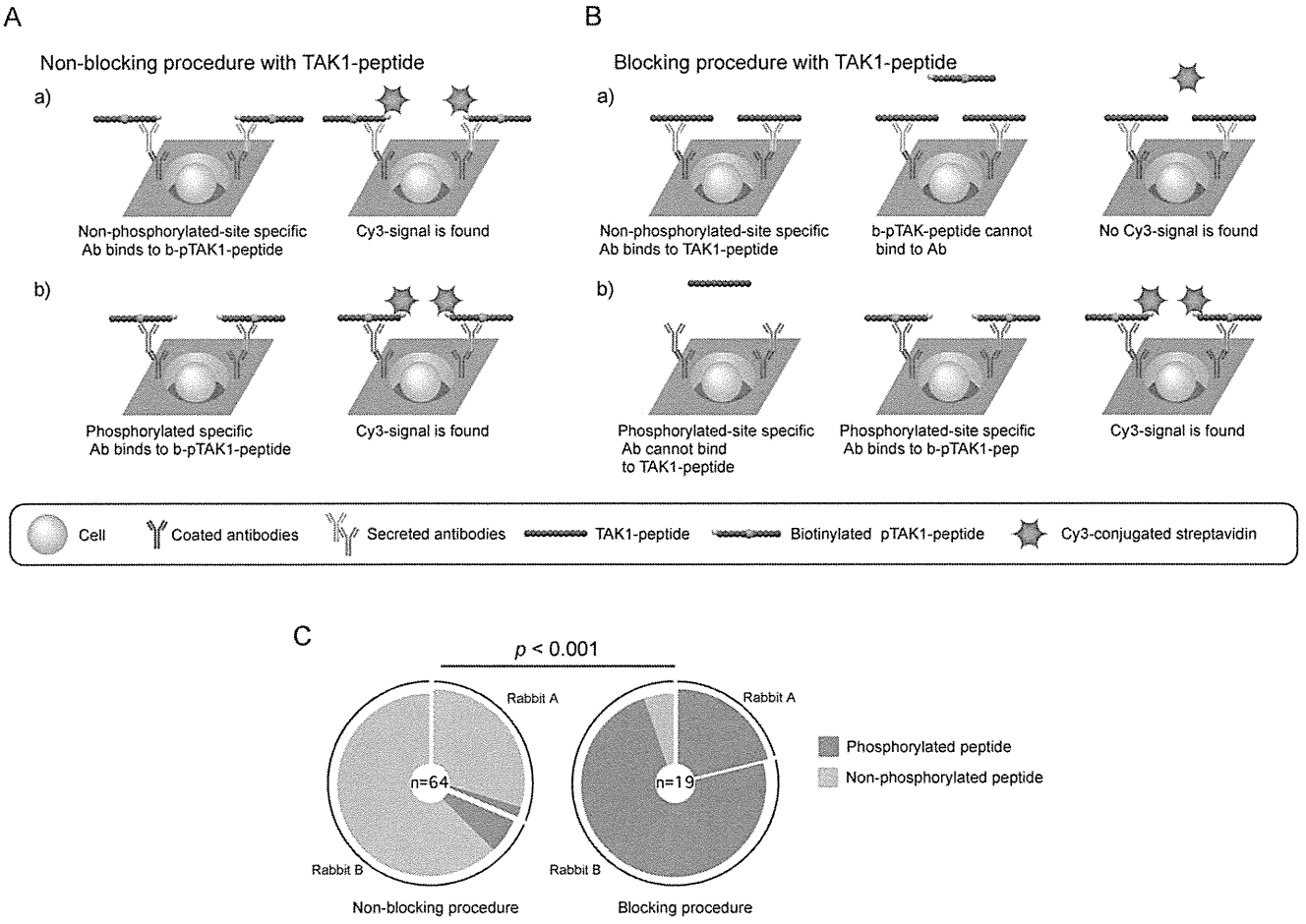

Figure 3. Efficient screening for phosphorylated peptide-specific RaMoAbs with rabbit-ISAAC. (A) Non-blocking procedure using the TAK1-peptide. Antibodies recognizing the non-phosphorylated peptide (a) and the phosphorylated peptide (b) can bind to biotinylated pTAK1-peptide, and a signal can be detected. (B) Blocking procedure using the TAK1-peptide. Microwell array chips were pre-treated with TAK1-peptide before the addition of biotinylated pTAK1-peptide. a) The TAK1-peptide binds to antibodies that recognize the non-phosphorylated site of the pTAK1-peptide. As a result, the biotinylated pTAK1-peptide cannot bind to the antibodies, and no signal is detected. b) The TAK1-peptide does not bind to antibodies that recognize the phosphorylated site of the pTAK1-peptide. As a result, the biotinylated pTAK1-peptide binds to antibodies, and a signal can be detected. (C) Acquisition efficiency of phosphorylated peptide-specific antibodies in the non-blocking and blocking procedures. The colored pie segment indicates the frequency of RaMoAbs that are specific to a phosphorylated peptide (red) and non-phosphorylated peptide (blue) in the non-blocking procedure (left) and the blocking procedure (right). The number in the center of the pie chart denotes the number of antibodies analyzed. The *p*-value was determined using Fisher's test.
doi:10.1371/journal.pone.0052383.g003

Table 2. Characterization of pTAK1-peptide-specific RaMoAbs.

Rabbit	ID	IGHV	IGHD	IGHJ	IGKV	IGKJ	Frequency[a]	*K*D (M)[b]
A	Ra_pTAK01	1S44	1	3	1S19	1–2	3	6.13×10^{-6}
A	Ra_pTAK04	1S44	7	2	1S56	1–2	1	2.76×10^{-9}
A	Ra_pTAK05	1S44	4	3	1S2	1–2	1	3.26×10^{-9}
B	Ra_pTAK06	1S44	7	4	1S2	1–2	8	1.15×10^{-9}
B	Ra_pTAK14	1S44	8	4	1S46 or 60	1–2	5	2.30×10^{-6}
B	Ra_pTAK19	1S44	1	2	1S12	1–2	2	2.06×10^{-9}
B	Ra_pTAK21	1S44	1	2	1S52	1–2	2	5.64×10^{-9}
B	Ra_pTAK23	1S44	7	4	1S2	1–2	1	1.23×10^{-9}

[a]Frequency indicates numbers of clones showing the identical amino acid sequences.
[b]The data are presented as average of at least two experiments.
doi:10.1371/journal.pone.0052383.t002

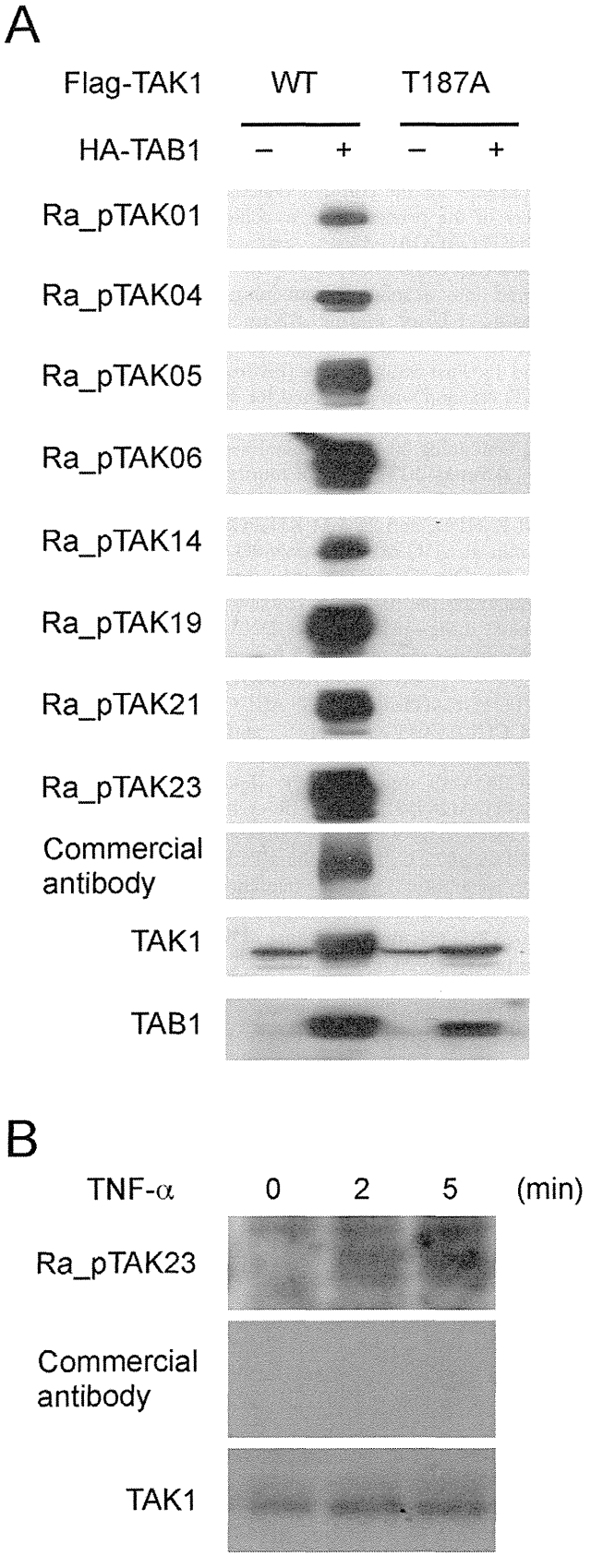

Figure 4. Western blot analysis of pTAK1-peptide-specific RaMoAbs. (A) Examination of the specificity of pTAK1-peptide-specific RaMoAbs. Whole-cell lysates obtained from HeLa cells that were transfected with plasmids containing FLAG-tagged wild type (WT) TAK1 or a phosphorylation site-substituted mutant (T187A) together with HA-tagged TAB1 were separated by SDS-PAGE and immunoblotted with Ra_pTAK01, 04, 05, 06, 14, 19, 21, and 23 antibodies, a commercial antibody specific to phosphorylated TAK1, a TAK1-specific antibody or a TAB1-specific antibody. (B) TNF-α-induced phosphorylation of endogenous TAK1 at Thr187. Whole cell lysates from HeLa cells that had been stimulated with 20 ng ml^{-1} TNF-α for the indicated time periods were separated by SDS-PAGE and immunoblotted with the Ra_pTAK23 antibody, a commercial pTAK1-pep-specific antibody, or a TAK1-specific antibody.
doi:10.1371/journal.pone.0052383.g004

case of pTAK1-peptide, a total of approximately 7.8×10^5 IgG^+ cells were analyzed using 24 microwell array chips. In all, approximately 590 TAK1/pTAK1-specific immunospots were detected, and 272 single cells were retrieved. From them, 128 pairs of V_H and V_L cDNAs were amplified and 118 RaMoAbs were produced. Finally, 64 of them specifically bound to TAK1/pTAK1 (Table S1). These results demonstrated the feasibility of ISAAC system for the analysis of antigen-specific ASC in rabbits and the comprehensive production of antigen-specific RaMoAbs.

A high affinity is one of the critical parameters for the selection of potent and efficacious therapeutic antibodies [28–31]. In this study, we analyzed the relationship between the sizes of the immunospots elicited by RaMoAbs produced by ASCs and their affinities. We found that the immunospots of antibodies with high affinity had smaller $D_{1/2}$ values compared to immunospots of antibodies with low affinity (Figure 2C and 2D); this is likely because high affinity antibodies quickly bind to antigen near the well and do not diffuse distantly. This result is accordance with the study of Adams *et al.* [23], which showed that antibodies with high affinity do not diffuse distantly in tumors. These results illustrate that we can efficiently screen for ASCs that produce high affinity RaMoAbs by selecting ASCs that produce immunospots with smaller $D_{1/2}$values. This screening procedure allows us to efficiently obtain antibodies with high affinities.

RaMoAbs with high affinities are useful for laboratory investigations and have many attractive features, including the ability to directly use reagents developed for western blot analysis that are substantially more sensitive. In this study, we showed that the RaMoAbs against HEL with 10^{-12} M affinity could detect 25-fold lower amount of the antigen compared to the mouse MoAbs that were obtained by mouse ISSAC (Figure S2). We also demonstrated that RaMoAb to pTAK1-peptide obtained by rabbit ISSAC detected endogenous phosphorylated TAK1 in TNFα-stimulated cells (Figure 4B). These data indicate that use of rabbit ISSAC system may contribute to the development of antibodies for not only laboratory use for clinical diagnosis but also researches in the field of signal transduction in cancer and inflammatory diseases, as well as Toll-like receptor signaling pathway.

We have demonstrated an efficient screening system for the procurement of phosphorylated peptide-specific ASCs using a blocking procedure (Figure 3). The acquisition efficiency was less than 10% using a non-blocking procedure; however, using a blocking procedure, the acquisition efficiency was extremely high (greater than 90%) (Figure 3). Thus, the rabbit-ISAAC system can be used to efficiently obtain a large panel of phosphorylation site-specific RaMoAbs, which may contribute to phosphoproteomic analyses in cell physiology [32,33] and in tumorigenesis [34]. Furthermore, the blocking procedure used in the rabbit-ISAAC system may assist in obtaining antibodies that recognize subtle changes in epitopes or modified epitopes such as amino acid substitution, acetylation, or glycosylation.

In conclusion, the rabbit-ISAAC system is a groundbreaking technological advancement that produces RaMoAbs with high affinity and specificity within a time period of only 7 days. This system may greatly promote the high-throughput production of RaMoAbs for laboratory research and clinical applications.

Materials and Methods

Antigens and Peptides

We used hen egg lysozyme (HEL; Sigma), bovine serum albumin (BSA; Wako), human transforming growth factor-β-activated kinase 1 (TAK1)-peptide (TAK1-peptide, DIQTHMNNKGSAA; Operon Biotechnologies), TAK1-peptide phosphorylated at Thr-187 (pTAK1-peptide, DIQTHM(pT)NNKGSAA; Operon Biotechnologies), biotinylated pTAK1-peptide (DIQTHM(pT)NNKGSAAK-biotin; Operon Biotechnologies), and KLH conjugates of pTAK1-peptide (Operon Biotechnologies).

Immunization of Rabbits and Cell Preparation

Experiments using rabbits were approved by the Committee on Animal Experiments at the University of Toyama. We immunized 12- to 13-week-old New Zealand White rabbits (Sankyo Lab) subcutaneously with 500 μg of HEL or KLH conjugates of pTAK1-peptide in complete Freund's adjuvant (Millipore). Two, four, and six weeks after primary immunization, we boosted the rabbits subcutaneously with 500 μg of the same material used in the primary immunization in incomplete Freund's adjuvant (Millipore). One week after the final boost, we isolated PBLs by centrifugation on a Ficoll–Hypaque gradient and isolated rabbit IgG^+ cells with rabbit IgG-specific antibody-conjugated microbeads (Miltenyi Biotec) using an autoMACS Pro separator (Miltenyi Biotec) according to the manufacturer's instructions.

Detection of Rabbit ASCs with a Microwell Array Chip (ISAAC)

The ISAAC method is covered by patents that have been exclusively licensed to Vivalis (Nantes, France). Details and instructions regarding the microwell array chip and the ISAAC method have been previously described [16,17,35–38]. Briefly, to detect HEL-specific IgG secretion, we coated the surface of the chip with 10 μg ml^{-1} HEL in phosphate-buffered saline (PBS) and incubated it overnight at 4°C. After removing the antigen solution, we blocked the chip with 0.01% Biolipidure (NOF Corporation, Japan) for 15 min at room temperature and subsequently washed it with the culture medium. We then arrayed cells in culture medium to the chip and removed residual cells outside the wells with gentle washing. We cultured the cells on the chip for 3 h at 37°C. After gentle washing, we applied 1.5 μg ml^{-1} of Cy3-conjugated rabbit IgG-specific goat polyclonal antibody (Millipore) to the chip and incubated for 30 min at room temperature to detect antigen-specific IgG secretion. To detect pTAK1-peptide-specific IgG secretion, we coated the surface of the chip with 1 μg ml^{-1} of rabbit IgG-specific antibody (MP Biomedicals) to trap secreted IgG. After the cells were cultured on the chip for 3 h, we added 10 μg ml^{-1} biotinylated pTAK1-peptide and incubated for 30 min; this was followed by the addition of Cy3-conjugated streptavidin (Sigma) for 30 min. Where indicated, we added 10 μg ml^{-1} TAK1-peptide to the chip and incubated for 30 min before adding biotinylated pTAK1-peptide. Finally, we stained the cells with 1 μM Oregon Green (Molecular Probes) for 5 min at room temperature. Antigen-specific antibodies that were released from single cells were observed under a fluorescence microscope (BX51WI, Olympus).

Production of RaMoAbs

We retrieved single antigen-specific ASCs from individual wells using a micromanipulator (TransferMan NK2, Eppendorf) fitted with capillaries (Primetech, Japan) under a fluorescence microscope and expelled them into micro-tubes containing a cell lysis solution composed of 30 μg of Dynabead $Oligo(dT)_{25}$ (Invitrogen), 3 μl of Lysis/Binding Buffer (Invitrogen), and 0.25 pmol of each specific primer for the constant regions of rabbit γ and κ. The sequences of the primers were as follows: Igγ (5′-GCGAGTA-GAGGCCTGAGGAC-3′) and Igκ (5′-GATGC-CAGTTGTTTGGGTGGT-3′). The Dynabeads were then transferred into a solution containing 15 U of SuperScriptIII (Invitrogen), 1 U of murine RNase inhibitor (New England Biolabs), 0.5 mM of each dNTP, 5 mM DTT, 0.2% Triton X-100, and 1× First Strand Buffer (Invitrogen). A reverse transcription (RT) reaction was performed for 40 min at 50°C. After the RT reaction, the Dynabeads were transferred into another solution containing 20 U of terminal deoxynucleotidyl transferase (Roche), 0.5 mM dGTP, 1 U of murine RNase inhibitor, 4 mM $MgCl_2$, 0.2% Triton-X 100, and 50 mM potassium buffer (25 mM K_2HPO_4 and 25 mM KH_2PO_4, pH 7.0), and incubated for 40 min at 37°C to add a poly-dG tail to the 3′ end of the cDNA. The Dynabeads were then transferred into a new PCR tube containing the first PCR reaction mix. The first PCR was performed using primeSTAR DNA polymerase (TaKaRa) according to the manufacturer's instructions with a dC adaptor primer (5′-AGCAGTAGCAGCAGTTCGATAACTTC-GAATTCTGCAGTCGACGGTACCGCGGGCCCGG-GATCCCCCCCCCCCCCDN-3′) and a specific primer for the constant region of rabbit γ (Igγ-1st: 5′-CGAGTTCCAAGT-CACGGTCA-3′) and rabbit κ (Igκ-1st: 5′-CTCCCAGGT-GACGGTGACAT-3′). The PCR cycles were as follows: 5 min at 95°C followed by 30 cycles of 15 sec at 95°C, 5 sec at 55°C, and 1 min 30 sec at 72°C. The resultant PCR mixtures were diluted 4-fold with water, and 2 μl of the dilution was added to 23 μl of the nested PCR mix to serve as template DNA. The nested PCR was performed in a reaction mix similar to the first PCR mix using an adaptor primer (5′-AGCAGTAGCAGCAGTTCGATAA-3′) and a specific primer for the constant region of rabbit γ (Igγ-nest: 5′-GCCTTTGACCAAGCAGCCCAA-3′) or rabbit κ (Igκ-nest: 5′-CGGGAAAGTATTTATTCGCCACA-3′). The PCR cycles were as follows: 5 min at 95°C followed by 35 cycles of 15 sec at 95°C, 5 sec at 55°C, and 1 min 30 sec at 72°C. We inserted the PCR products into expression vectors that contained cDNAs for the whole constant region of rabbit γ or κ chains. Thereafter, we co-transfected CHO-S cells (Invitrogen) with both the γ and κchain expression vectors encoding whole antibody molecules using the FreeStyle MAX CHO Expression System (Invitrogen), and we collected the supernatants of cultured cells after 3 days. We examined the antigen specificity of the recombinant antibodies by ELISA and confirmed the results with competitive ELISA by adding soluble antigen to the antibodies [17,36]. In this study, we screened only IgG-secreting cells with ISAAC. The immunoglobulin gene repertoire was analyzed with the IMGT/V-Quest tool (http://www.imgt.org/) [39]. For the determination of antibody affinity and western blotting, we collected the supernatants of cultured cells after 7 days and purified the RaMoAbs using a protein G column (GE Healthcare).

Determination of Antibody Affinity

We determined antibody affinities (*K*D) at antibody-antigen equilibrium (Ab+Ag ↔ AbAg) in solution [40,41]. Briefly, we incubated various concentrations (0.2, 1, or 10 nM) of HEL-specific monoclonal antibodies with 0.3 to 1,000 nM of HEL or 1

to 2,500 nM pTAK1-peptide overnight at 4°C until equilibrium was reached. We then measured the concentrations of free antibody that remained unsaturated with antigens at equilibrium by ELISA and calculated *K*D using Scatchard plot analysis. To this end, we coated 96-well MaxiSorp™ plates (Nunc) with 50 µl per well of 5 µg ml^{-1} HEL or 2.5 µg ml^{-1} pTAK1-peptide in PBS and subsequently blocked with 3% BSA in PBS. After washing, we added the mixture of antigen and antibodies at equilibrium to the plates and incubated for 1 h at room temperature. We detected antibodies that were unsaturated with antigens using IgG-specific antibodies conjugated to alkaline phosphatase and *p*-nitrophenyl-phosphate, and we measured the optical absorbance at 405 nm with an ELISA reader. From the optical absorbance, we calculated the concentration of antibody that was unsaturated with antigen [Abf] and the concentration of antigen that was not bound to antibody [Agf].

Determination of LOD in ELISA

Ninety-six-well Maxisorp plates were coated with 50 µl per well of 1 µg ml^{-1} of IgG-specific antibody in PBS and then blocked with 3% BSA in PBS. After washing, 30 pM of the rabbit HEL-specific antibody was added to the plate and incubated for 1 hr at room temperature. The plate was washed with PBS-T three times, and various concentrations (100 to 0.1 pM) of biotinylated HEL were added to the plates and then incubated for 1 hr at room temperature. The binding of HEL was detected using 0.5 µg ml^{-1} of alkaline phosphatase labeled-streptavidin (Sigma) and *p*-nitrophenylphosphate. The optical absorbance was measured at 405 nm with an ELISA reader, according to the manufacturer's instructions. LOD were determined by extrapolating the concentration from the signal equal to background signal plus 3 s.d.

Western Blotting

We used a TAK1 antibody (M-579; Santa Cruz Biotechnology), a TAB1 antibody (C-20; Santa Cruz Biotechnology), and a phospho-TAK1 (Thr187) antibody (#4536; Cell Signaling Technology). We transfected HeLa cells with FLAG-tagged TAK1 and HA-tagged TAB1 expression plasmids [25] using Lipofectamine reagents (Invitrogen). We stimulated HeLa cells with 20 ng ml^{-1} TNF-α (R&D Systems) for 2 and 5 min. After the stimulation, we prepared whole cell lysates with lysis buffer (25 mM HEPES pH 7.7, 0.3 M NaCl, 1.5 mM $MgCl_2$, 0.2 mM EDTA, 0.1% Triton X-100, 20 mM β-glycerophosphate, 1 mM sodium orthovanadate, 1 mM phenylmethylsulfonyl fluoride, 1 mM DTT, 10 µg ml^{-1} aprotinin, and 10 µg ml^{-1} leupeptin). We resolved the cell lysates by SDS-PAGE and transferred them to an Immobilon-P nylon membrane (Millipore). We treated the membrane with BlockAce (Dainippon Pharmaceutical Co.) and probed it with approximately 100 ng ml^{-1} of primary antibody as described above followed by horseradish peroxidase-conjugated anti rabbit or goat IgG-specific antibody (DAKO). Visualization was performed using the ECL system (GE Healthcare).

Supporting Information

Figure S1 Determination of affinity for HEL-specific RaMoAbs. Various concentrations (0.2, 1, or 10 nM) of HEL-specific RaMoAbs were incubated with 0.3 to 1,000 nM HEL overnight at 4°C until equilibrium was reached. The concentration of free antibody that remained unsaturated at equilibrium was then measured by ELISA using HEL-coated 96-well plates. The concentration (nM) of HEL is indicated on the *x*-axis, and the absorbance at 405 nm is indicated on the *y*-axis. Data are representative of at least two independent experiments with similar results. The data were used for determination of *K*D using Scatchard plots.
(TIF)

Figure S2 Determination of limit of detection of HEL in ELISA using rabbit and mouse HEL-specific antibodies. Biotinylated HEL ranged from 100 pM to 0.1 pM were used to examine the limit of detection (LOD) of HEL using rabbit or mouse HEL-specific antibodies that showed the highest affinity among the obtained antibodies. LOD of the rabbit (Ra_HEL01; *K*D 2.63×10^{-12} M) (left) and mouse (*K*D 3.71×10^{-10} M) (right) HEL-specific antibodies were 0.4 pM and 10 pM, respectively. LOD was determined by extrapolating the concentration from the signal equal to background signal plus 3 s.d. of the background signal. Blue and red dotted lines indicate LODs of rabbit and mouse, respectively. Data are a representative of three independent experiments with similar results.
(TIF)

Figure S3 Determination of affinity for pTAK1-peptide-specific RaMoAbs. Various concentrations (0.2 or 6 nM) of pTAK1-peptide-specific RaMoAbs were incubated with 1 to 2,500 nM pTAK1-peptide overnight at 4°C until the equilibrium was reached. The concentration of free antibody that remains unsaturated at equilibrium was measured by ELISA using pTAK1-peptide-coated 96-well plate. The concentration (nM) of pTAK1-peptide is indicated on the *x*-axis, and the absorbance at 405 nm is indicated on the *y*-axis. Data are representative of at least two independent experiments with similar results. The data were used for determination of *K*D using Scatchard plots.
(TIF)

Table S1 Efficiency of rabbit ISAAC for producing RaMoAbs.
(XLS)

Acknowledgments

We thank Sanae Hirota for technical assistance and Kaoru Hata for secretarial work.

Author Contributions

Conceived and designed the experiments: TO EK HS AJ HK AM. Performed the experiments: TO XP YZ TA. Analyzed the data: TO XP HS HK AM. Wrote the paper: TO HK AM.

References

1. Weller A, Meek J, Adamson ED (1987) Preparation and properties of monoclonal and polyclonal antibodies to mouse epidermal growth factor (EGF) receptors: evidence for cryptic EGF receptors in embryonal carcinoma cells. Development 100: 351–363.
2. Rossi S, Laurino L, Furlanetto A, Chinellato S, Orvieto E, et al. (2005) Rabbit monoclonal antibodies: a comparative study between a novel category of immunoreagents and the corresponding mouse monoclonal antibodies. Am J Clin Pathol 124: 295–302.
3. Huang Z, Zhu W, Meng Y, Xia H (2006) Development of new rabbit monoclonal antibody to progesterone receptor (Clone SP2): no heat pretreatment but effective for paraffin section immunohistochemistry. Appl Immunohistochem Mol Morphol 14: 229–233.
4. Mage RG, Lanning D, Knight KL (2006) B cell and antibody repertoire development in rabbits: the requirement of gut-associated lymphoid tissues. Dev Comp Immunol 30: 137–153.
5. Tao GZ, Nakamichi I, Ku NO, Wang J, Frolkis M, et al. (2006) Bispecific and human disease-related anti-keratin rabbit monoclonal antibodies. Exp Cell Res 312: 411–422.

6. Zhu W, Yu G-L (2009) Rabbit hybridoma. Therapeutic Monoclonal Antibodies: From Bench to Clinic (Zhiqiang An (Editor)) Hoboken, New Jersey: John Wiley & Sons.
7. Krause RM (1970) The search for antibodies with molecular uniformity. Adv Immunol 12: 1–56.
8. Bystryn JC, Jacobsen JS, Liu P, Heaney-Kieras J (1982) Comparison of cell-surface human melanoma-associated antigens identified by rabbit and murine antibodies. Hybridoma 1: 465–472.
9. Norrby E, Mufson MA, Alexander H, Houghten RA, Lerner RA (1987) Site-directed serology with synthetic peptides representing the large glycoprotein G of respiratory syncytial virus. Proc Natl Acad Sci U S A 84: 6572–6576.
10. Raybould TJ, Takahashi M (1988) Production of stable rabbit-mouse hybridomas that secrete rabbit mAb of defined specificity. Science 240: 1788–1790.
11. Feng L, Wang X, Jin H (2011) Rabbit monoclonal antibody: potential application in cancer therapy. Am J Transl Res 3: 269–274.
12. Kuo MC, Sogn JA, Max EE, Kindt TJ (1985) Rabbit-mouse hybridomas secreting intact rabbit immunoglobulin. Mol Immunol 22: 351–359.
13. Verbanac KM, Gross U, Rebellato LM, Thomas JM (1993) Generation of rabbit anti-lymphocyte monoclonal antibodies. Transplant Proc 25: 837–838.
14. Verbanac KM, Gross UM, Rebellato LM, Thomas JM (1993) Production of stable rabbit-mouse heterohybridomas: characterization of a rabbit monoclonal antibody recognizing a 180 kDa human lymphocyte membrane antigen. Hybridoma 12: 285–295.
15. Spieker-Polet H, Sethupathi P, Yam PC, Knight KL (1995) Rabbit monoclonal antibodies: generating a fusion partner to produce rabbit-rabbit hybridomas. Proc Natl Acad Sci U S A 92: 9348–9352.
16. Jin A, Ozawa T, Tajiri K, Obata T, Kishi H, et al. (2011) Rapid isolation of antigen-specific antibody-secreting cells using a chip-based immunospot array. Nat Protoc 6: 668–676.
17. Jin A, Ozawa T, Tajiri K, Obata T, Kondo S, et al. (2009) A rapid and efficient single-cell manipulation method for screening antigen-specific antibody-secreting cells from human peripheral blood. Nat Med 15: 1088–1092.
18. Ozawa T, Kishi H, Muraguchi A (2006) Amplification and analysis of cDNA generated from a single cell by 5′-RACE: application to isolation of antibody heavy and light chain variable gene sequences from single B cells. Biotechniques 40: 469–470, 472, 474 passim.
19. Ozawa T, Tajiri K, Kishi H, Muraguchi A (2008) Comprehensive analysis of the functional TCR repertoire at the single-cell level. Biochem Biophys Res Commun 367: 820–825.
20. Popkov M, Mage RG, Alexander CB, Thundivalappil S, Barbas CF, 3rd, et al. (2003) Rabbit immune repertoires as sources for therapeutic monoclonal antibodies: the impact of kappa allotype-correlated variation in cysteine content on antibody libraries selected by phage display. J Mol Biol 325: 325–335.
21. Raman C, Spieker-Polet H, Yam PC, Knight KL (1994) Preferential VH gene usage in rabbit Ig-secreting heterohybridomas. J Immunol 152: 3935–3945.
22. Winstead CR, Zhai SK, Sethupathi P, Knight KL (1999) Antigen-induced somatic diversification of rabbit IgH genes: gene conversion and point mutation. J Immunol 162: 6602–6612.
23. Adams GP, Schier R, McCall AM, Simmons HH, Horak EM, et al. (2001) High affinity restricts the localization and tumor penetration of single-chain fv antibody molecules. Cancer Res 61: 4750–4755.
24. Sakurai H (2012) Targeting of TAK1 in inflammatory disorders and cancer. Trends Pharmacol Sci. in press.
25. Singhirunnusorn P, Suzuki S, Kawasaki N, Saiki I, Sakurai H (2005) Critical roles of threonine 187 phosphorylation in cellular stress-induced rapid and transient activation of transforming growth factor-beta-activated kinase 1 (TAK1) in a signaling complex containing TAK1-binding protein TAB1 and TAB2. J Biol Chem 280: 7359–7368.
26. Sakurai H, Miyoshi H, Mizukami J, Sugita T (2000) Phosphorylation-dependent activation of TAK1 mitogen-activated protein kinase kinase kinase by TAB1. FEBS Lett 474: 141–145.
27. Shibuya H, Yamaguchi K, Shirakabe K, Tonegawa A, Gotoh Y, et al. (1996) TAB1: an activator of the TAK1 MAPKKK in TGF-beta signal transduction. Science 272: 1179–1182.
28. Lu D, Shen J, Vil MD, Zhang H, Jimenez X, et al. (2003) Tailoring in vitro selection for a picomolar affinity human antibody directed against vascular endothelial growth factor receptor 2 for enhanced neutralizing activity. J Biol Chem 278: 43496–43507.
29. Velders MP, van Rhijn CM, Oskam E, Fleuren GJ, Warnaar SO, et al. (1998) The impact of antigen density and antibody affinity on antibody-dependent cellular cytotoxicity: relevance for immunotherapy of carcinomas. Br J Cancer 78: 478–483.
30. Yu Y, Lee P, Ke Y, Zhang Y, Yu Q, et al. (2010) A humanized anti-VEGF rabbit monoclonal antibody inhibits angiogenesis and blocks tumor growth in xenograft models. PLoS One 5: e9072.
31. Zhu Z, Hattori K, Zhang H, Jimenez X, Ludwig DL, et al. (2003) Inhibition of human leukemia in an animal model with human antibodies directed against vascular endothelial growth factor receptor 2. Correlation between antibody affinity and biological activity. Leukemia 17: 604–611.
32. Giljohann DA, Mirkin CA (2009) Drivers of biodiagnostic development. Nature 462: 461–464.
33. Cui Y, Wei Q, Park H, Lieber CM (2001) Nanowire nanosensors for highly sensitive and selective detection of biological and chemical species. Science 293: 1289–1292.
34. Bao YP, Wei TF, Lefebvre PA, An H, He L, et al. (2006) Detection of protein analytes via nanoparticle-based bio bar code technology. Anal Chem 78: 2055–2059.
35. Tajiri K, Kishi H, Tokimitsu Y, Kondo S, Ozawa T, et al. (2007) Cell-microarray analysis of antigen-specific B-cells: single cell analysis of antigen receptor expression and specificity. Cytometry A 71: 961–967.
36. Tokimitsu Y, Kishi H, Kondo S, Honda R, Tajiri K, et al. (2007) Single lymphocyte analysis with a microwell array chip. Cytometry A 71: 1003–1010.
37. Kinoshita K, Ozawa T, Tajiri K, Kadowaki S, Kishi H, et al. (2009) Identification of antigen-specific B cells by concurrent monitoring of intracellular Ca2+ mobilization and antigen binding with microwell array chip system equipped with a CCD imager. Cytometry A 75: 682–687.
38. Ozawa T, Kinoshita K, Kadowaki S, Tajiri K, Kondo S, et al. (2009) MAC-CCD system: a novel lymphocyte microwell-array chip system equipped with CCD scanner to generate human monoclonal antibodies against influenza virus. Lab Chip 9: 158–163.
39. Giudicelli V, Chaume D, Lefranc MP (2004) IMGT/V-QUEST, an integrated software program for immunoglobulin and T cell receptor V-J and V-D-J rearrangement analysis. Nucleic Acids Res 32: W435–440.
40. Friguet B, Chaffotte AF, Djavadi-Ohaniance L, Goldberg ME (1985) Measurements of the true affinity constant in solution of antigen-antibody complexes by enzyme-linked immunosorbent assay. J Immunol Methods 77: 305–319.
41. Djavadi-Ohaniance L, Goldberg ME, Friguet B (1996) Antibody engineering (Eds : McCafferty J, et al) IRL Press, Oxford: 77–96.

Unbiased Analysis of TCRα/β Chains at the Single-Cell Level in Human CD8$^+$ T-Cell Subsets

Xiaoming Sun[1], Masumichi Saito[1], Yoshinori Sato[1], Takayuki Chikata[1], Takuya Naruto[1], Tatsuhiko Ozawa[2], Eiji Kobayashi[2], Hiroyuki Kishi[2], Atsushi Muraguchi[2], Masafumi Takiguchi[1]*

1 Center for AIDS Research, Kumamoto University, Honjo, Kumamoto, Japan, **2** Department of Immunology, Graduate School of Medicine and Pharmaceutical Sciences, University of Toyama, Toyama, Japan

Abstract

T-cell receptor (TCR) α/β chains are expressed on the surface of CD8$^+$ T-cells and have been implicated in antigen recognition, activation, and proliferation. However, the methods for characterization of human TCRα/β chains have not been well established largely because of the complexity of their structures owing to the extensive genetic rearrangements that they undergo. Here we report the development of an integrated 5′-RACE and multiplex PCR method to amplify the full-length transcripts of TCRα/β at the single-cell level in human CD8$^+$ subsets, including naive, central memory, early effector memory, late effector memory, and effector phenotypic cells. Using this method, with an approximately 47% and 62% of PCR success rate for TCRα and for TCRβ chains, respectively, we were able to analyze more than 1,000 reads of transcripts of each TCR chain. Our comprehensive analysis revealed the following: (1) chimeric rearrangements of TCRδ-α, (2) control of TCRα/β transcription with multiple transcriptional initiation sites, (3) altered utilization of TCRα/β chains in CD8$^+$ subsets, and (4) strong association between the clonal size of TCRα/β chains and the effector phenotype of CD8$^+$ T-cells. Based on these findings, we conclude that our method is a useful tool to identify the dynamics of the TCRα/β repertoire, and provides new insights into the study of human TCRα/β chains.

Citation: Sun X, Saito M, Sato Y, Chikata T, Naruto T, et al. (2012) Unbiased Analysis of TCRα/β Chains at the Single-Cell Level in Human CD8$^+$ T-Cell Subsets. PLoS ONE 7(7): e40386. doi:10.1371/journal.pone.0040386

Editor: George Kassiotis, MRC National Institute for Medical Research, United Kingdom

Received January 31, 2012; **Accepted** June 6, 2012; **Published** July 6, 2012

Funding: This research was supported by the Global COE program "Global Education and Research Center Aiming at the control of AIDS" (No. F13), launched as a project commissioned by the Ministry of Education, Science, Sports, and Culture, Japan (http://www.jsps.go.jp/english/e-globalcoe/01_outline.html). The funders had no role in study design, data collection and analysis, decision to publish, or preparation of the manuscript.

Competing Interests: The authors have declared that no competing interests exist.

* E-mail: masafumi@kumamoto-u.ac.jp

Introduction

CD8$^+$ T cells play an important role in adaptive immunity against virus-infected cells and tumor cells [1–3]. In the primary antigen response, naive CD8$^+$ T cells are activated in secondary lymph nodes and consequently undergo clonal expansion and differentiation into effector and memory CD8$^+$ cells that sequentially circulate in the periphery in vivo [4,5]. Effector CD8$^+$ T cells have direct effector functions such as cytotoxic activity and cytokine production in response to the target cells, whereas memory CD8$^+$ T cells do not show these functions, but have the ability to proliferate and secrete large amounts of cytokines when the cells are stimulated by antigens [6].

T-cell receptor (TCR)α/β chains are heterodimeric membrane proteins expressed on the surface of CD8$^+$ T-cells, and they contribute to direct recognition of antigen peptide presented on the major histocompatibility complex (MHC) in the target cells [7,8]. The specificity of antigen recognition for diverse peptide-MHC (pMHC) complexes depends on the 3 complementarity determining regions (CDRs) of both TCRα and TCRβ chains. CDR1 and CDR2 are encoded by the germline sequences and mainly used for the binding to the MHC, whereas CDR3 is known to be the highly polymorphic and the principal antigen recognition site created by extensive genomic rearrangement occurring among variable (V), diversity (D), and joining (J) segments. The diversity of CDR3 is further generated by the deletion and insertion of nucleotides within the junction of V-J and V-D-J in TCRα and TCRβ chains, respectively [9–11].

Methods to characterize the diversity and clonality of the TCRα/β repertoire have been previously described and remarkably improved by the development of recent technologies such as TCR spectratyping [12–14] and deep sequencing [15–18]. However, most approaches have focused on the characterization of a single TCRβ chain without consideration of the TCRα/β pairs that determine the actual TCR diversity and clonotype. There are some methods that have been described for the analysis of paired TCRα/β chain transcripts from single cells, but these methods are limited to activated human T-cells *in vitro* or antigen-specific mouse T-cells *ex vivo* [19–21].

The TCR amplification methods are basically categorized into 2 groups based on the utilization of the 5′rapid amplification of cDNA end (RACE) method [22] or the multiplex PCR method [23]. The 5′-RACE method can exclude potential bias and provide full-length TCRα/β transcripts that are useful for sequential study such as that of TCRα/β transduction, which analyzes the specificity of an antigen. However, the specificity and efficiency of PCR amplification in the 5′-RACE method are low, especially when there is contamination by short fragments created by mRNA degradation or incomplete cDNA synthesis in the reverse transcription process. In contrast, the multiplex PCR method gives better specificity and efficiency of PCR than the 5′-

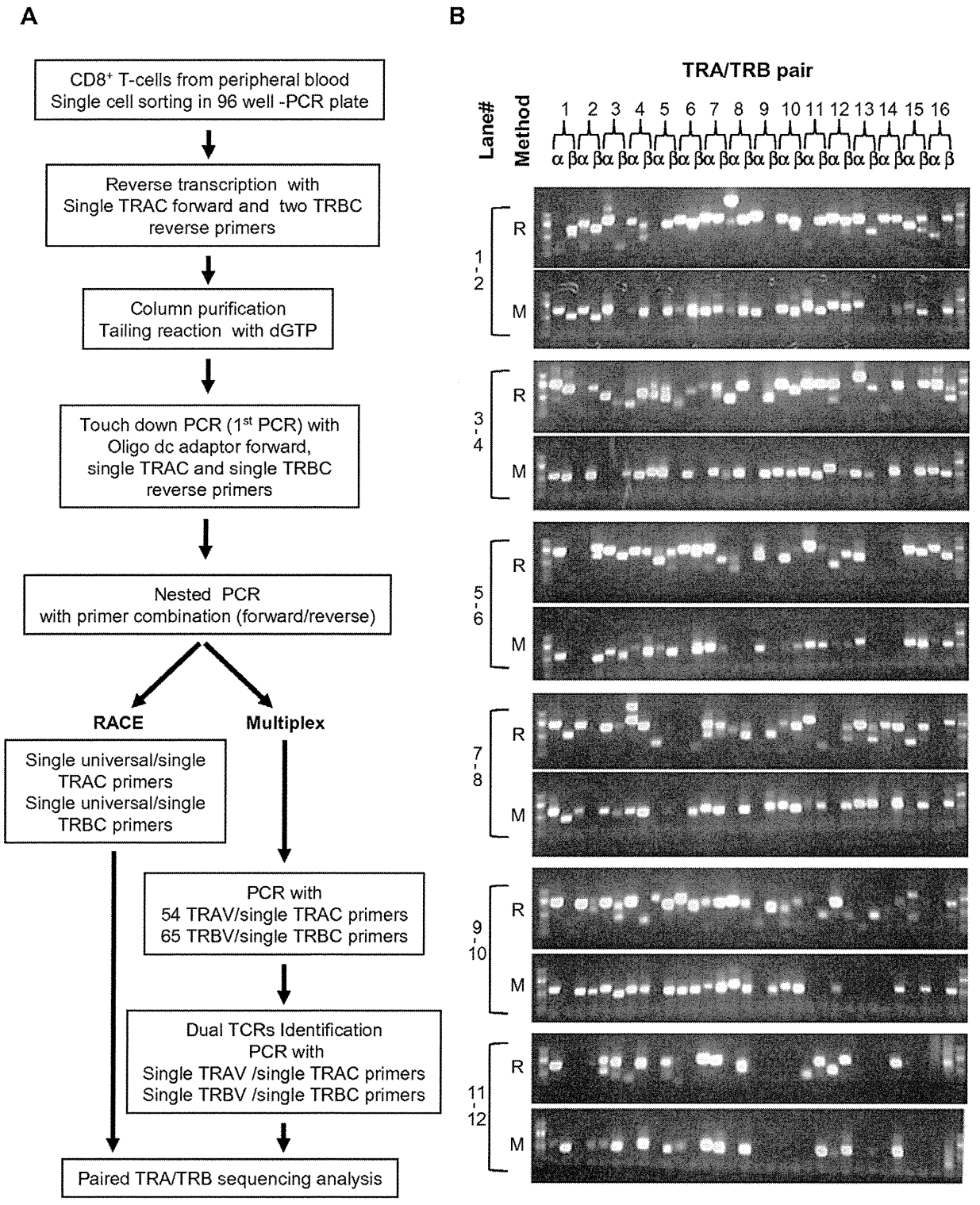

Figure 1. Amplification of TCRα/β chains from single CD8+ T-cells. (A) Experimental strategy for amplifying and sequencing TCRα/β chains by integrated 5′-RACE (RACE) and multiplex PCR (Multiplex). (B) Visualization of TCRα/β chain transcripts by agarose gel electrophoresis. The results were obtained from 96 cells in the naive subset in donor 1 and are shown as a representative result. R: 5′-RACE, M: mutitiplex PCR.
doi:10.1371/journal.pone.0040386.g001

RACE method but does not provide the full length of TCRα/β transcripts. In addition, it potentially has bias because of multiple primers designed for each variable segment of TCRα/β chains.

Here, we report an unbiased method developed by the integration of 5′RACE and multiple PCR methods for amplification of the full-length and paired TCRα/β chain transcripts at the single cell level in human CD8+ T-cell subsets. This method

has wide applications and has allowed us to demonstrate chimeric rearrangements in TCRα/β chains, regulation of TCRα/β chain expression with multiple transcriptional initiation sites, and dynamics of the TCRα/β repertoire among different subsets of human $CD8^+$ T cells.

Results

Amplification of full-length TCRα/β chain transcripts from single $CD8^+$ T-cells

We applied the integrated 5′-RACE and multiplex PCR method for amplification of the full length of both TCRα and TCRβ chain transcripts from single cells in $CD8^+$ T-cell subsets including naive ($CD27^{high}CD28^+CD45RA^+CCR7^+$), central memory ($CD27^+CD28^+CD45RA^-CCR7^+$), early effector memory ($CD27^+CD28^+CD45RA^-CCR7^-$), late effector memory ($CD27^{low}CD28^-CD45RA^{+/-}CCR7^-$), and effector ($CD27^-CD28^-CD45RA^{+/-}CCR7^-$) phenotypic populations obtained from the peripheral blood of 3 unrelated donors (Table 1) [24]. The PCR amplifications were successfully performed (Figure 1), and the overall PCR success rate was approximately 47% for TCRα and 62% for TCRβ chains. This result is consistent with a previous report indicating that the PCR success rate for TCRβ chains is slightly better than that for TCRα chains in mice [19]. Although the results of PCR amplification given by 5′-RACE and multiplex PCR methods were almost identical, as shown in Figure 1B, a subset of TCRα/β chain transcripts appeared once from either 5′-RACE or and multiplex PCR method. These results indicate that the integration of 5′-RACE and multiplex PCR methods could increase the PCR success rate. Indeed, we selected 1250 samples for analysis (974 samples from 5′RACE and 276 samples from Multiplex PCR method) for TCRα chain and 1661 samples (1075 samples from 5′RACE and 586 samples from Multiplex PCR method) for TCRβ chain (Table S1). Form these data, we found that approximately 80% of TCRα and 87% of TCRβ chains were in-frame and that approximately 16% of TCRα chains and 6% of TCRβ chains were out of frame. Among the chains, 3.4% of TCRα ones and 5.8% of TCRβ ones were germline transcripts that lacked the variable segments and showed unproductive TCRs (Figure 2A and 2B) [25,26]. All germline transcripts were detected by 5′ RACE, but not by the multiplex PCR method. A fraction of samples failed to identify the TCR because of unreadable sequences, which may indicate the existence of dual TCRs. Therefore, we performed PCR with a single gene-specific primer designed for the middle of the variable region in the TCRα/β chains, and the sequence analysis revealed that productive dual TCRα and TCRβ chains were expressed in approximately 1.9% and 0.8% of $CD8^+$ T-cells, respectively (Figure 2C and 2D). Approximately 14% of $CD8^+$ T-cells had only unproductive TCRα (Fig2A and C), though productive TCRβ chain was detected in a half of these cells. We did not clarify whether these cells express only TCRβ chain because success rate to detect TCRα chain by this method is approximately 50%. Furthermore, consistent with a previous report [19], the most frequent dual TCRα and TCRβ were observed with a combination of productive TCR and unproductive TCR, the latter of which had either a stop codon or frame-shift.

Since CDR3 is the most diverse region, created by the deletion and insertion of nucleotides within the junction of V-J and V-D-J in TCRα and TCRβ chains, respectively, we analyzed the distribution of CDR3 length at the amino acid (aa) level in TCRα and TCRβ chains by using samples showing only productive TCR defined by the in-frame sequence (1,011 and 1,444 reads for TCRα and TCRβ chains, respectively). The analysis demonstrated that the length of CDR3α ranged from 4 to 18 aa, whereas the length of CDR3β was slightly longer, ranging from 5 to 20 aa (Figure 2E). Further analysis of paired CDR3α and CDR3β lengths with 736 samples identified the most frequent pair at the position intersecting 11 and 13 aa of CDR3α and CDR3β lengths, respectively (Figure 2F). These results suggest that human TCRα/β chains may have a preferential combination of CDR3α and CDR3β lengths for recognition of diverse pMHC complexes.

Identification of transcriptional initiation sites (TISs) in genes of TCRα/β chains

Our integrated method included 5′-RACE, which is able to amplify the full length of transcripts and has been used to identify the TIS of genes. Therefore, we examined whether our sequence data obtained from single cells also had the power to identify the TISs of TCRα/β chains. At first we collected samples that showed the presence of a translational initiation site in TCRα/β chains, and then the sequences were aligned with the genomic sequences to measure the length of the 5′-UTR (5′-untranslated region) that eventually informs the position of the TCRα/β TISs. With 773 and 930 reads for TCRα and TCRβ chains, respectively, the distribution of TISs in the genes of TCRα/β chains showed that the TISs of the TCRβ chain accumulated around 40-bp downstream of the translational initiation sites but that those of the TCRα chain were concentrated in 2 locations, i.e., 40 bp and 110 bp downstream of the translational initiation sites (Figure 3A). The TISs in individual TCRα/β variable segment (TRAV and TRBV) were also analyzed, and the results showed that subsets of TRAV and TRBV transcripts started from more than 2 positions (Figure 3B and 3C), suggesting that there are multiple binding sites for transcription factors that tightly control the expression of TCRα/β chains restricted in T lymphocytes [27,28].

Usage of TCRα/β variable segments in human $CD8^+$ T-cell subset

To analyze the usage of TRAVs and TRBVs in human $CD8^+$ T-cell subset, we extracted samples including the variable segments but not those identified as germline transcripts from the whole sequence data set. The assembly of the samples obtained from 1,207 and 1,540 reads for TCRα and TCRβ chains, respectively (Table S2), demonstrated that 42 out of 54 TRAVs and 47 out of 64 TRBVs were detected in the $CD8^+$ T-cell subset with different frequencies but that all pseudogenes except TRBV21-1 were not detectable (Figure 4A and 4B). The IMGT data base together with a previous report [15] has defined TRBV21-1 as a pseudogene based on the fact that it has a frame-shift in the leader sequence, but about 30% of our samples carrying the TRBV21-1 rearrangement appeared as productive TCRβ chains encoding CDR1, CDR2, and CDR3 domains with in-frame sequences in the entire transcript (data not shown), suggesting that TRBV21-1 may function and be required for antigen recognition *in vivo*. There were several TRBV segments that were not detected in this analysis. Interestingly, we found TRDV-TRAJ rearrangement in a substantial number of TCRα transcripts (Figure S1). These results, along with the finding of TRBV21-1 utilization, define the requirement of the 5′-RACE method and the limitation of the multiplex PCR method if multiple primers are designed for variable segments in TCRα/β chains.

Using the same data set, we next analyzed the usage of TRAVs and TRBVs in each $CD8^+$ subset among 3 unrelated donors (Figure 4C and 4D). The results indicated that the usage of

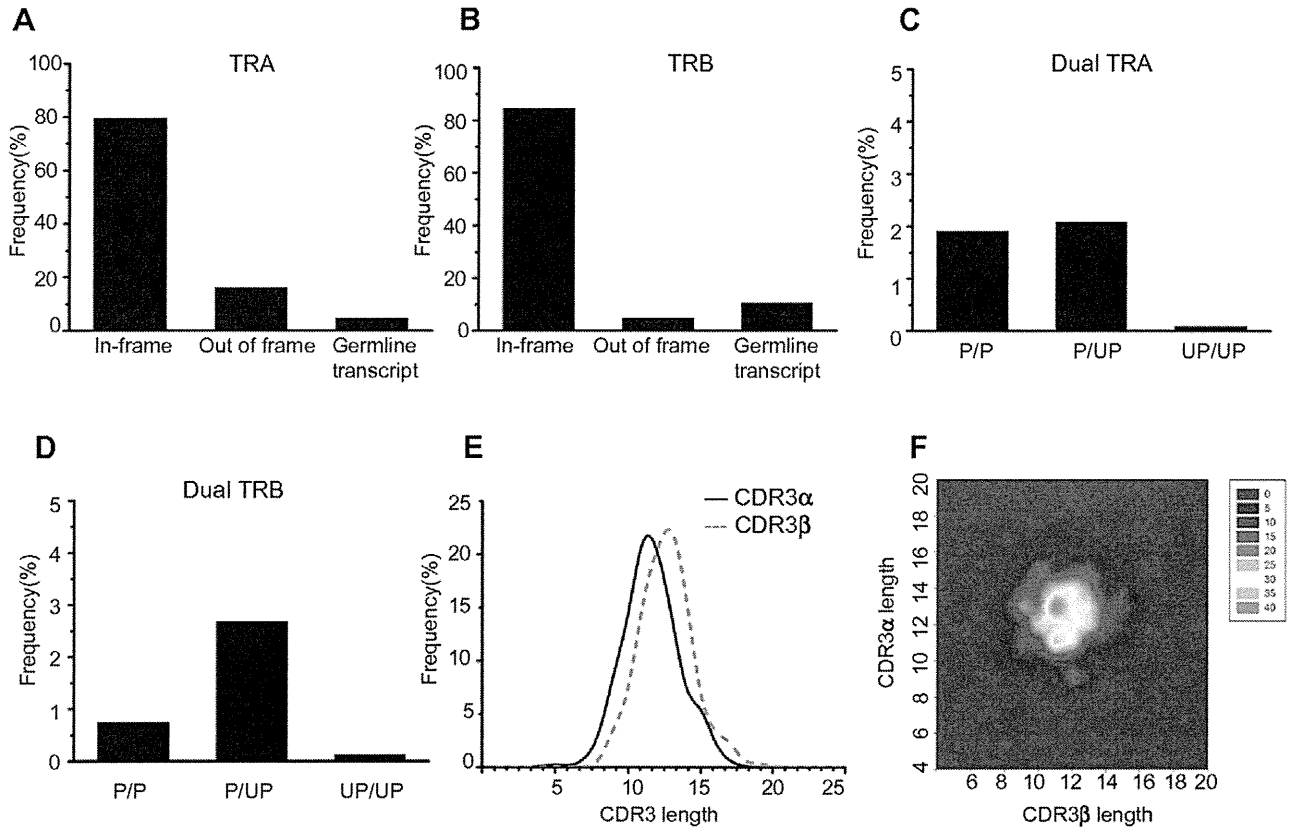

Figure 2. Characterization of TCRα/β-chain transcripts expressed in CD8+ T-cells. For characterization of TCRα/β chain transcripts, 1,250 and 1,661 sequence reads were used for TCRα and TCRβ chains, respectively. (A) Frequency of in-frame, out-of-frame, and germline transcripts for TCRα chains. Out-of-frame transcripts represent a sequence that contains either a stop codon or a frame-shift, whereas germline transcripts are defined by the absence of a variable segment and evidence that the transcript was started from a genomic region located in the upstream of either a joining or diversity segment. (B) Frequency of in-frame, out-of-frame, and germline transcripts for TCRβ chains. (C) Frequency of dual TCRα chain transcripts. The samples that had 2 transcripts were defined as dual TCRs. P: productive TCRs representing in-frame transcripts. UP: unproductive TCRs representing out-of-frame transcripts. (D) Frequency of dual TCRβ-chain transcripts. (E) Size distribution of CDR3α and CDR3β lengths. Samples representing productive TCRs (1,011 and 1,444 reads for TCRα and TCRβ chains, respectively) were extracted from the whole data set. The CDR3 lengths were identified by the IMGT/V-Quest tool at the amino acid (aa) level. (F) Paired analysis of CDR3α and CDR3β lengths. By use of 736 samples, the most frequent pair was identified at the position intersecting 11 and 13 aa of CDR3α and CDR3β lengths, respectively, as shown in red.
doi:10.1371/journal.pone.0040386.g002

TRAV1-2 in all of the donors was significantly higher in the early effector memory cells than in other 3 subsets and that the usage of TRAV8-3 was significantly higher in naïve subset than in other 3 subsets (Figure 4C). The usage of TRBV12-3 was significantly lower in early effector memory subset than in late effector memory subset while that of TRBV2 was significantly higher in naïve subset than in effector subset (Figure 4D). Furthermore, the detailed analysis of TRAV1-2 showed that most TRAV1-2 had rearranged with TRAJ33 and that CDR3α was highly conserved among samples and also among donors (Figure S2 and Table S3). In addition, the paired TCRα/β analysis showed that the TRBV6 subgroup was preferentially used for the pairing with TRAV1-2-TRAJ33 rearranged within the TCRα chain.

Usage of joining and diversity segments of TCRα/β chains in human CD8+ T-cell subset

The analysis of usage of joining and diversity segments (TRAJ, TRBJ, and TRBD) was performed on the same data set as used for the TRAV and TRBV usage analysis. The result showed that 51 out of 61 TRAJs and 13 out of 14 TRBJs in TCRα/β chains were detected with different frequencies in the CD8+ T-cell subset of the 3 donors (Figure 5A and 5B). Consistent with the observation made by TRAV and TRBV usage analysis, we found that several joining segments defined as pseudogenes were not detectable in any of the CD8+ T-cell subsets. There was no significant difference in the usage of TRBD1 and TRBD2 among the 3 donors (Figure 5C). We observed that a subset of TCRα/β chain transcripts lacked TRAJ, TRBJ or TRBD. This result suggests that the transcripts lacking TRAJ and TRBJ may have been due to splicing errors and that the lack of TRBD may have been a consequence of deletion of its nucleotides during the process of V-D-J recombination.

To analyze the usage of TRAJ and TRBJ in each CD8+ subset among the 3 unrelated donors, we used the same data set. The analysis demonstrated that the usage of TRBJ1-1 was significantly higher in naïve subset than in early effector memory and effector subsets (Figure 5E).

Identity and clonotype of TCRα/β chains in human CD8+ T-cell subset

Given the fact that antigen-experienced CD8+ T-cells clonally proliferate after activation and sequentially differentiate into memory phenotypic CD8+ T-cells that circulate in the periphery *in vivo*, it is possible that the identity and clonotype of TCRα/β

Table 1. Success rate of single-cell PCR for TCRα/β chains in CD8+ T-cell subsets.

	Donor 1					Donor 2					Donor 3				
Age	26					34					29				
Sex	Male					Male					Male				
HLA type	A*31:01/A*31:01/B*40:06/B*56:01/C*04:01/C*08:01					A*01:01/A*24:02/B*37:01/B*40:02/C*03:03/C*06:02					A*02:01/A*24:02/B*51:01/B*52:01/C*12:02/C*04:01				
CD8+T-cell subset	N	CM	EEM	LEM	E	N	CM	EEM	LEM	E	N	CM	EEM	LEM	E
Population (%)	46.3	1.64	17.0	2.12	5.97	67.9	1.17	9.14	1.06	2.87	47.1	0.74	8.47	5.24	19.9
Total # of cells analyzed for TRA	92	77	74	82	67	90	75	75	72	83	90	74	81	87	84
PCR success rate for TRA (%)	63.9	68.8	61.7	56.9	39.9	45.8	39.1	19.5	37.5	43.2	62.5	38.5	42.2	45.3	43.8
Total # of cells analyzed for TRB	119	90	86	92	98	118	132	106	105	102	115	108	109	111	113
PCR success rate for TRB (%)	82.6	80.4	71.7	63.9	58.3	61.5	68.8	27.6	54.7	53.1	79.9	56.3	56.8	57.8	58.9

doi:10.1371/journal.pone.0040386.t001

chains may be in different proportions among CD8+ T-cell subsets. To examine this possibility, we at first analyzed the identity of TCRα and TCRβ chains individually in each CD8+ T-cell subset by using the same data set as used for the TRAV and TRBV usage analysis. The results showed that the identity of both TCRα and TCRβ chains had gradually increased from naive cells to effector cells, which had been phenotypically classified beforehand (Figure 6A and 6B) [24]. In addition, approximately 60% of effector cells showed identical TCRα/β chains once at least, suggesting the occurrence of clonal expansion *in vivo*. Using a data set that provided the paired TCRα/β chain transcripts (901 paired sequence reads), we next analyzed the clonotype of TCRα and TCRβ chains by satisfying the following requirements for the different samples in each CD8+ T-cell subset of the 3 donors: (1) identical usage of variable, diversity, and joining segments in TCRα/β chains and (2) perfect matching of CDR3 length and sequence at the amino acid level in TCRα/β chains. The analysis revealed that the largest proportion of clonotype was the effector subset, with none or a smaller proportion of it as naive, central memory, early effector memory or late effector memory subset (Figure 6C). This result shows that the clonal size of CD8+ T-cells was associated with the effector phenotype, as had been previously described and classified by the degree of expression of 3 effector molecules [24]. Further analysis demonstrated that the number, type, and size of TCRα/β clonotypes were different among the donors having different HLA-types with the exception of the HLA-A*24:02 type in donor 2 and donor 3 (Figure 6D and Table S4), suggesting that the cells showing the TCRα/β clonotype were clonally expanded after activation by the recognition of different pMHC complexes *in vivo*.

Discussion

The methods for TCR amplification have been previously reported and continuously improved by the development of recent technology [12–16,18–21]. However, we were unable to find any suitable method for our analysis based on our requirements, such as the amplification of full-length and paired TCRα/β chains from human CD8+ T-cells at the single cell level with high PCR success rate and no potential bias. Hence, we newly developed an integrated method originating from 5′-RACE and multiplex PCR methods. We found that our method successfully worked across human CD8+ T-cell subsets obtained from 3 unrelated individuals without a reduction in PCR success rate compared with that obtained with methods previously described [19,21]. In the comprehensive TCRα/β analysis, the necessity of our integrated method was emphasized by the following evidence: 1) a subset of TCRα/β chain transcripts was amplified with either the 5′-RACE or multiplex PCR method, 2) the 5′-RACE, but not multiplex PCR, method could amplify germline transcripts and transcripts carrying the chimeric rearrangements of TCRδ-TCRα 3) the combination of multiplex PCR and sequential PCR with single TRAV or TRBV primers identified the existence of dual TCR expression in single CD8+ T-cells. In light of this evidence, we expect that the full-length of paired TCRα/β chain transcripts amplified by the 5′-RACE method will be useful for not only the identification of transcription initiation sites, but also for simplifying the strategy of TCRα/β tranduction to confirm the pairing and potential antigen recognition through the direct cloning into lenti-virus expression vectors, as described previously [29].

The regulation of mono- or bi-allelic expression at TCR and immmunoglobulin (Ig) loci is known to involve changes in chromatin structure, methylation, and replication timing in 2 identical alleles [30–33]. In our data set, about 80% of CD8+ T-cells showed mono-allelic expression of TCRα and TCRβ chains, with expression of dual TCRα and dual TCRβ in approximately 3% of them. However, a previous study demonstrated that dual TCRα expression, but not dual TCRβ expression, was detected in 10~20% of influenza-specific peripheral CD8+ T-cells [19], suggesting that the difference in the frequency of dual TCR may depend on the type of cells targeted. Indeed, we found that 9.2% of early effector cells from the donor 1 expressed dual TCRα

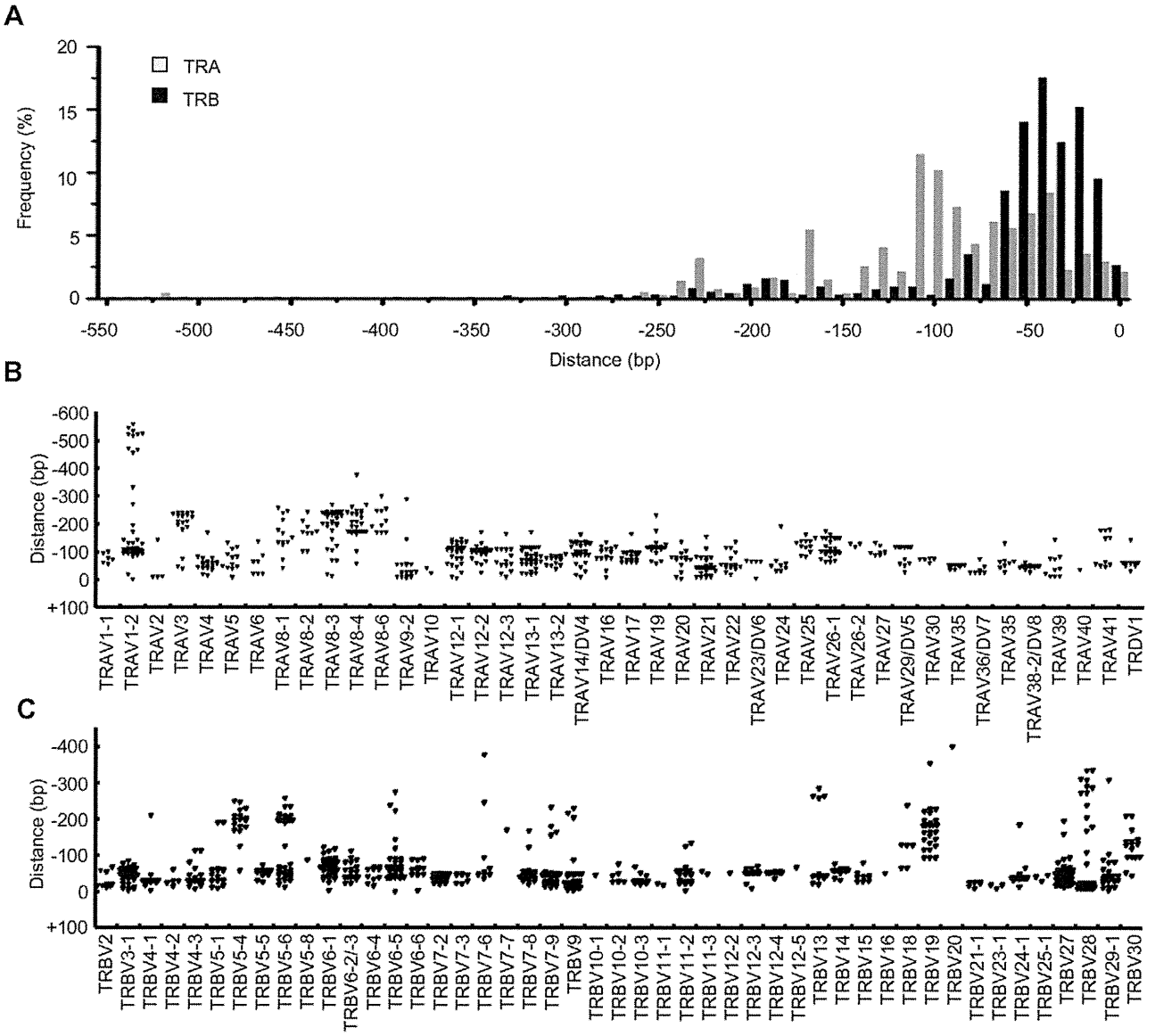

Figure 3. Identification of transcription initiation sites (TISs) in TCRα/β chain. (A) Distribution of TISs in TCRα/β chains. Samples containing a translation initiation site (773 and 930 reads for TCRα and TCRβ chains, respectively) were used for the analysis, and the initiation site was defined as zero. (B) Distribution of TISs in TRAVs of TCRα chains. Using the same data set, TISs were determined for individual TRAVs. (C) Distribution of TISs in TRBVs of TCRβ chains. A single dot represents a position of TIS obtained from a single sequence read.
doi:10.1371/journal.pone.0040386.g003

chains with single TCRβ chains and that there was no association between CD8+ T-cell subsets and the frequency of dual TCRs among the 3 unrelated donors.

The germilne transcription coding for unproductive TCR and Ig composed of D-J-C or J-C segments has been found to occur before the V(D)J rearrangement, and is thought to be driven by a developmental stage-specific promoter that should be activated in immature cells [25,26,34]. A striking observation in our data was the expression of germline transcripts in peripheral CD8+ T-cells, where we found that most of these transcripts were detected together with a productive TCR transcript in a subset of CD8+ T-cells. This finding, together with the result that approximately 80% of the CD8+ T-cells analyzed in this study expressed a single TCR support the idea that these germline transcripts were expressed in immature T-cells by biallelic activation at D or J locus, but that only 1 of the 2 alleles was inactivated in mature T-cells after V-(D)-J rearrangement through methylation and the changes in chromatin structure. Some of the mature T-cells analyzed escaped in this manner.

TISs have been investigated in murine and human TCRβ chains, with the finding that the positions fall into a range of 19–40 bp and 26 bp upstream of the translation initiation site in most murine TRBVs and human TRBV7-2 (Vβ6.7), respectively [27,28]. These results are consistent with ours in that the positions of TISs were located quite close to the translational initiation site. However, our finding that there were multiple transcription sites in a subset of TRBVs as well as TRAVs, and the fact that the promoters located in each TRBV did not have uniform transcriptional activity, suggests that the regulatory mechanism of TCRα/β expression may be more complicated and that these events may be implicated in the usage of variable segments in TCRα/β chains in CD8+ T-cell subsets.